https://doi.org/10.5194/essd-2020-123
Preprint. Discussion started: 7 July 2020

Open Access Earth System Science Data Discussions

Carbon Monitoring System Flux Net Biosphere Exchange 2020 (CMS-Flux NBE 2020)

Junjie Liu[1,2*], Latha Baskaran[1], Kevin Bowman[1], David Schimel[1], A. Anthony Bloom[1], Nicholas C. Parazoo[1], Tomohiro Oda[3,4], Dustin Carroll[5], Dimitris Menemenlis[1], Joanna Joiner[3], Roisin Commane[6], Bruce Daube[7], Lucianna V. Gatti[8], Kathryn McKain[9,10], John Miller[9], Britton B. Stephens[11], Colm Sweeney[9], Steven Wofsy[7],

1. Jet Propulsion Laboratory, Caltech, CA
2. Caltech, CA
3. Global Modeling and Assimilation Office, NASA Goddard Space Flight Center, Greenbelt, MD
4. Goddard Earth Sciences Technology and Research, Universities Space Research Association, Columbia, MD
5. Moss Landing Marine Laboratories, San José State University, California, CA
6. Lamont-Doherty Earth Observatory of Columbia University, NY
7. Harvard University, Cambridge, MA
8. LaGEE, CCST, INPE- National Institute for Space Researc, Brazil
9. NOAA, Global Monitoring Laboratory, Boulder, CO 80305
10. University of Colorado, Cooperative Institute for Research in Environmental Sciences, Boulder, CO
11. National Center for Atmospheric Research, Boulder, CO 80301

Correspondence: Junjie Liu (junjie.liu@jpl.nasa.gov)

Abstract. Here we present a global and regionally-resolved terrestrial net biosphere exchange (NBE) dataset with corresponding uncertainties between 2010–2018: CMS-Flux NBE 2020. It is estimated using the NASA Carbon Monitoring System Flux (CMS-Flux) top-down flux inversion system that assimilates column CO_2 observations from Greenhouse gases Observing SATellite (GOSAT) and the NASA's Observing Carbon Observatory -2 (OCO-2). The regional monthly fluxes are readily accessible as tabular files, and the gridded fluxes are available in NetCDF format. The fluxes and their uncertainty estimates are evaluated by extensively comparing the posterior CO_2 mole fractions with aircraft CO_2 observations. We describe the characteristics of the dataset as global total, regional climatological mean, and regional annual fluxes and seasonal cycles. We find that the global total fluxes of the dataset agree with atmospheric CO_2 growth observed by the surface-observation network within uncertainty. Averaged between 2010 and 2018, the tropical regions range from close-to neutral in tropical South America to a net source in Africa; these contrast with the extra-tropics, which are a net sink of 2.5 ± 0.3 gigaton carbon per year. The regional satellite-constrained NBE estimates provide a unique perspective for understanding the terrestrial biosphere carbon dynamics and monitoring changes in regional contributions to the changes of atmospheric CO_2 growth rate. The gridded and regional aggregated dataset can be accessed at: https://doi.org/10.25966/4v02-c391 (Liu et al., 2020).

1 Introduction

New "top-down" inversion frameworks that harness satellite observations provide an important complement to global aggregated fluxes (e.g., Global Carbon Project, Friedlingstein et al., 2019) and inversions based on surface CO_2 observations (e.g., Crowell et al., 2019). These satellite-constrained estimates resolve regional fluxes, and also disentangle net biosphere exchange (NBE) into constituent carbon fluxes including plant gross primary productivity (GPP) and biomass burning through solar-induced fluorescence and carbon monoxide proxies, respectively (Bowman et al, 2017, Liu et al., 2017). Both the spatial and process resolution are critical for evaluating models and reducing uncertainties about future carbon-climate feedbacks (e.g., Friedlingstein et al., 2014). The NBE are far more variable than ocean fluxes (Lovenduski and Bonan, 2017) or fossil fuel emissions (Yin et al, 2019), and are thus the focus of this dataset estimated from a top-down atmospheric CO_2 inversion of satellite column CO_2 dry-air mole fraction (X_{CO2}). We present the global and regional NBE dataset as a series of maps, time series and tables, and disseminate it as a public dataset for further analysis and comparison to other sources of flux information. Finally, we provide a comprehensive evaluation of both mean and uncertainty estimates against an independent airborne dataset. Subsequent papers will present the partitioning of the NBE into constituent gross fluxes.

Global top-down atmospheric CO_2 flux inversions have been historically used to estimate regional terrestrial NBE, which is a sum of net ecosystem exchange and biomass burning carbon fluxes. They make uses of the spatiotemporal variability of atmospheric CO_2, which is dominated by NBE, to infer net carbon exchange at the surface (Chevallier et al., 2005; Baker et al., 2006; Liu et al., 2014). The accuracy of the NBE from top-down flux inversion is determined by the density and

https://doi.org/10.5194/essd-2020-123
Preprint. Discussion started: 7 July 2020

accuracy of the CO_2 observations, the accuracy of modeled atmospheric transport, and knowledge of the prior uncertainties of the flux inventories.

For CO_2 flux inversions based on high precision *in situ* and flask observations, the measurement error is low (<0.2 parts per million (ppm)) and not a significant source of error; however, these observations are limited spatially, and are concentrating primarily over North America (NA) and Europe (Crowell et al., 2019). Satellite X_{CO2} from CO_2-dedicated satellites, such as the Greenhouse Gases Observing Satellite (GOSAT) (launched in July 2009) and the Observing Carbon Observatory 2 (OCO-2) (Crisp et al., 2017) have much broader spatial coverage (O'Dell et al., 2018), and fill the observational gaps of conventional surface CO_2 observations, but they have up to an order of magnitude higher single-sounding uncertainty and potential systematic errors compared to the *in situ* and flask CO_2 observations. Recent progress in instrument error characterization, spectroscopy, and retrieval methods have significantly improved the accuracy and precision of the X_{CO2} retrievals (O'Dell et al., 2018; Kiel et al., 2019). The single sounding random error of X_{CO2} from OCO-2 is ~1.0 ppm (Kulawik et al., 2019). A recent study by Byrne et al. (2020) shows less than a 0.5 ppm difference between posterior X_{CO2} constrained by a recent data set, ACOS-GOSAT b7 X_{CO2} retrievals, and those constrained by conventional surface CO_2 observations. Chevallier et al. (2019) also showed that OCO-2 based flux inversion had similar performance to surface CO_2 based flux inversions when comparing posterior CO_2 mole fractions to aircraft CO_2 in the free troposphere. Results from these studies show that systematic uncertainties in CO_2 retrievals from satellites are comparable to, or smaller than, other uncertainty sources in atmospheric inversions (e.g. transport).

https://doi.org/10.5194/essd-2020-123
Preprint. Discussion started: 7 July 2020

A newly-developed biogeochemical model-data fusion system, CARDAMOM, made progress in producing NBE uncertainties, along with mean values that are consistent with a variety of observations assimilated through a Markov Chain Monte Carlo (MCMC) method (Bloom et al., 2016; 2020). Transport model errors in general have also been reduced relative to earlier transport model intercomparison efforts, such as TRANSCOM 3 (Gurney et al., 2004; Gaubert et al., 2019). Advancements in satellite retrieval, transport, and prior terrestrial biosphere modeling have led to more mature inversions constrained by satellite X_{CO2} observations.

Two satellites, GOSAT and OCO-2, have now produced more than 10 years of observations. Here we harness the CMS-Flux inversion framework (Liu et al., 2014; 2017; 2018; Bowman et al., 2017) to generate an NBE product: CMS-Flux NBE 2020, by assimilating both GOSAT and OCO-2 from 2010–2018. The dataset is the longest satellite-constrained NBE product so far. The CMS-Flux framework exploits globally available X_{CO2} to infer spatially-resolved total surface-atmosphere exchange, which can be subsequently decomposed into individual fluxes using ancillary measurements (i.e., GPP, respiration, fires, fossil fuel, etc.). The flux estimates from the CMS-Flux framework have been used to assess the impacts of El Niño on terrestrial biosphere fluxes (Bowman et al, 2017; Liu et al, 2017) and the role of droughts in the North America (NA) carbon balance (Liu et al, 2018). These fluxes have furthermore been ingested into land-surface data assimilation systems to quantify heterotrophic respiration (Konings et al., 2019), evaluate structural and parametric uncertainty in carbon-climate models (Quetin et al., 2020), and inform climate dynamics (Bloom et al., 2020). We present the regional NBE and its uncertainty based on two types of regional masks: (1) latitude and continent; and)2) distribution of biome types (defined

https://doi.org/10.5194/essd-2020-123
Preprint. Discussion started: 7 July 2020

by plant functional types), and continent. The gridded NBE dataset and its uncertainty are also available, so that users can aggregate the fluxes and uncertainties based on self-defined regions.

The outline of the paper is as follows: Section 2 describes methods, and Sections 3 and 4 describe the dataset and the major NBE characteristics, respectively. We extensively evaluate the posterior fluxes and uncertainties by comparing the posterior CO_2 mole fractions against aircraft observations and a gross primary production (GPP) product (section 5). In Section 6, we discuss the strength and weakness, and potential usage of the data. A summary is provided in Section 7, and Section 8 is dataset availability and future plan.

2 Methods

2.1 CMS-Flux inversion system

The CMS-Flux framework is summarized in Figure 1. The center of the system is the CMS-Flux inversion system, which optimizes NBE and air-sea net carbon exchanges with a 4D-Var inversion system (Liu et al., 2014). In the current system, we assume that no uncertainty in fossil fuel emissions, since the uncertainty in fossil fuel emissions at regional scales is substantially less than NBE uncertainties, which is a widely adopted assumption in global flux inversion systems (e.g., Crowell et al., 2019). The 4D-Var minimizes a cost function that include the sum of two terms:

$$J(\mathbf{x}) = (\mathbf{x}-\mathbf{x}_b)^T \mathbf{B}^{-1}(\mathbf{x}-\mathbf{x}^b) + (\mathbf{y}-h(\mathbf{x}))^T \mathbf{R}^{-1}(\mathbf{y}-h(\mathbf{x})) \quad (1)$$

The first term measures the differences between the optimized fluxes and the prior fluxes normalized by the prior flux error covariance $\mathbf{B}$, and the second term measures the differences between observations ($\mathbf{y}$) and the corresponding model simulated value ($h(\mathbf{x})$) normalized by the observation error covariance $\mathbf{R}$. The term $h(\cdot)$ is the observation operator that calculates

https://doi.org/10.5194/essd-2020-123
Preprint. Discussion started: 7 July 2020

observation-equivalent model-simulated X_{CO2}. The 4D-Var uses the adjoint (i.e., the backward integration of the transport model) (Henze et al., 2004) of the GEOS-Chem transport model to calculate the sensitivity of the observations to surface fluxes. The configurations of the inversion system are summarized in Table 1. We run both the forward and adjoint at 4° x 5° spatial resolution, and optimize monthly NBE and air-sea carbon fluxes at each grid point from January 2010 to December 2018. Inputs for the system include prior carbon fluxes, meteorological drivers, and the satellite X_{CO2} (Figure 1). Section 2.2 (Table 2) describes the prior flux and its uncertainties, and section 2.3 (Table 3) describes the observations and the corresponding uncertainties.

2.2 The prior CO_2 fluxes and uncertainties

Prior CO_2 fluxes include NBE, air-sea net carbon fluxes, and fossil fuel emissions (see Table 2). The data sources for the prior fluxes are listed in Table 7. Methods to generate prior ocean carbon fluxes and fossil fuel emissions are documented in Brix et al., (2015), Caroll et al. (2020), and Oda et al. (2018). The focus of this dataset is optimized terrestrial biosphere fluxes, so we briefly describe the prior terrestrial biosphere fluxes and its uncertainties.

We construct the NBE prior using the CARDAMOM framework (Bloom et al., 2016). CARDAMOM data assimilation system explicitly represents the time-resolved uncertainties in NBE. The prior estimates are already constrained with multiple data streams accounting for measurement uncertainties following a similar Bayesian approach used in the 4D-variational approach. We use the CARDAMOM setup as described by Bloom et al. (2016, 2020) resolved at monthly timescales; data constraints include GOME-2 solar-induced fluorescence (Joiner et al., 2013), MODIS Leaf Area Index (LAI), and biomass and soil carbon (details on the data

https://doi.org/10.5194/essd-2020-123
Preprint. Discussion started: 7 July 2020

assimilation are provided in Bloom et al. (2020)). In addition, mean GPP and fire carbon emissions from2010 - 2017 are constrained by FLUXCOM GPP (Tramontana et al., 2016) and GFEDv4.1s (Randerson et al., 2018) respectively, both assimilated with an uncertainty of 20%. We use the Olsen and Randerson (2001) approach to downscale monthly GPP and respiration fluxes to 3-hourly timescales, based on ERA-interim re-analysis of global radiation and surface temperature. Fire fluxes are downscaled using the GFEDv4.1 daily and diurnal scale factors on monthly emissions (Giglio et al., 2013). Posterior CARDAMOM NBE estimates are then summarized as NBE mean and standard deviation values.

The NBE from CARDAMON shows net carbon uptake of 2.3 GtC/year over the tropics and close to neutral in the extratropics (Figure S1). The year-to-year variability (i.e., interannual variability, IAV) estimated from CARDAMOM from 2010 –2017 is generally less than 0.1 gC/m^2/day outside of the tropics (Figure S1). Because of the weak interannual variability estimated by CARDAMOM, we use the same 2017 NBE prior for 2018.

CARDAMOM generates uncertainty along with the mean state. The relative uncertainty over the tropics is generally larger than 100%, and the magnitude is between 50% and 100% over the extra-tropics (Figure S2). We assume no correlation in prior flux errors in either space or time. Temporal and spatial error correlation estimates can in principle be computed by CARDAMOM. We anticipate incorporating these error correlations in subsequent versions of this dataset.

2.3 Column CO_2 observations from GOSAT and OCO-2

We use satellite-column CO_2 retrievals from Atmospheric Carbon Observations from Space (ACOS) team for both GOSAT (version 7.3) and OCO-2 (version 9) (Table 3). The use of the same retrieval algorithm and validation strategy adopted by ACOS team to process both GOSAT and OCO-2 spectra maximize the consistency between these two datasets. Both GOSAT and OCO-2 satellites carry high-resolution spectrometers optimized to return high precision measurements of reflected sunlight within CO_2 and O_2 absorption bands in the shortwave infrared (Crisp et al., 2012). Both satellites fly in a sun-synchronous orbit. GOSAT has a 13:00 ± 0.15 hours local crossing time and a three-day ground track repeat cycle. The footprint of GOSAT is ~10.5 km in diameter in sun-nadir view (Crisp et al., 2012). The daily number of soundings processed by the ACOS-GOSAT retrieval algorithm is between a few hundreds to ~2000. Further quality control and filtering reduce the ACOS-GOSAT X_{CO2} retrievals to 100 – 300 daily (Figure S5 in Liu et al., 2017). We only assimilate ACOS-GOSAT land nadir good quality observations.

OCO-2 has a 13:30 local crossing time and 16-day ground track repeat cycle. The nominal footprints of OCO-2 are 1.25 km wide and ~2.4 km along the orbit. Because of its small footprint and sampling strategy, OCO-2 has many more X_{CO2} retrievals than ACOS-GOSAT. OCO-2 has four observing modes: land nadir, land glint, ocean glint, and target. Following Liu et al. (2017), we only use land nadir observations from OCO-2 to generate a set of super observations by aggregating the observations within ~100 km (along the same orbit). The super observations have more uniform spatial coverage and are more comparable to the spatial representation of ACOS-GOSAT observations (see Figure S5 in Liu et al., 2017).

We directly use observational uncertainty provided with ACOS-GOSAT b7.3 to represent the observation error, **R**, in Eq 1. The uncertainty of the OCO-2 super observations is the sum of the variability of X_{CO2} used to generate each individual super observation and the mean uncertainty

https://doi.org/10.5194/essd-2020-123
Preprint. Discussion started: 7 July 2020

provided in the original OCO-2 retrievals. More detailed information about OCO-2 super observations can be found in Liu et al. (2017). Kulawik et al. (2019) showed that both OCO-2 and ACOS-GOSAT bias-corrected retrievals have mean biases of -0.1 ppm when compared against X_{CO2} from Total Carbon Column Observing Network (TCCON) (Wunch et al., 2011), indicating consistency between ACOS-GOSAT and OCO-2 retrievals. The magnitude of observation errors used in **R** is generally above 1.0 ppm, larger than the sum of random error and biases in the observations. The ACOS-GOSAT b7.3 observations from July 2009–June 2015 are used to optimize fluxes between 2010 and 2014, and the OCO-2 X_{CO2} observations from Sep 2014–June 2019 are used to optimize fluxes between 2015 and 2018.

The observational coverage of ACOS-GOSAT and OCO-2 is spatiotemporally dependent, with more coverage during summer than winter over the NH, and more observations over mid-latitudes than over the tropics (Figure S3). The variability (i.e., standard deviation) of annual total number of observations from 2010–2014 is within 4% of the annual mean number for ACOS-GOSAT. Except for a data gap in 2017 caused by a malfunction of OCO-2 instrument, the variability of annual total number of observations between 2015 and 2018 is within 8% of the annual mean number for OCO-2.

2.4 Uncertainty quantification

The posterior flux error covariance is analytically the inverse Hessian, which incorporates the transport, measurement, and background errors at the 4D-Var solution (Eq. 13 in Bowman et al, 2017). For large-order systems, the posterior errors cannot be explicitly calculated. Consequently, we rely on a Monte Carlo approach to quantify posterior flux uncertainties following Chevallier et al. (2010) and Liu et al. (2014). In this approach, an ensemble of flux inversions is carried out with

https://doi.org/10.5194/essd-2020-123
Preprint. Discussion started: 7 July 2020

an ensemble of priors and simulated observations to sample the uncertainties of prior fluxes (i.e., **B** in eq. 1) and observations (**R** in Eq. 1), respectively. The magnitude of posterior flux uncertainties is a function of assumed uncertainties in prior fluxes and observations, as well as the density of observations. Since the density of GOSAT and OCO-2 observations are stable (section 2.3) within their respective data record, we characterize the posterior flux uncertainties for 2010 and 2015 only, and assume the flux uncertainties for 2011–2014 are the same as 2010 and flux uncertainties for 2016–2018 are the same as 2015.

2.5 Evaluation of posterior fluxes

Direct NBE estimates from flux towers only provide a spatial representation of a few kilometers (Running et al., 1999), not appropriate to evaluate regional NBE from top-down flux inversions. Thus, we use two methods to indirectly evaluate the posterior NBE and its uncertainties. One is to compare annual NBE anomalies and seasonal cycle to a gross primary production (GPP) product. The other is to compare posterior CO_2 mole fractions to independent aircraft observations (i.e., not assimilated in the inversion). The second method has been broadly used to indirectly evaluate posterior fluxes from top-down flux inversions (e.g., Stephens et al., 2007; Liu and Bowman, 2016; Chevallier et al., 2019; Crowell et al., 2019).

2.5.1 Evaluation against independent gross primary production (GPP) product

NBE is a small residual difference between two large terms: total ecosystem respiration (TER) and GPP, plus fire. A positive NBE anomaly (i.e., less uptake from the atmosphere) has been shown to correspond to reduced GPP caused by climate anomalies (e.g., Bastos et al., 2018), and the magnitude of net uptake is proportional to GPP in most biomes observed by flux tower observations (e.g, Falk et al., 2008). Since NBE is related not only to GPP, the comparison to GPP only serves as a qualitative measure of the NBE quality. For example, we would expect that the

https://doi.org/10.5194/essd-2020-123
Preprint. Discussion started: 7 July 2020

posterior NBE seasonality to be anti-correlated with GPP in the temperate and high latitudes. In this study, we use FLUXSAT GPP (Joiner et al., 2018), which is an upscaled GPP product based on flux tower GPP observations and satellite-based geometry adjusted reflectance from the MODerate-resolution Imaging Spectroradiometer (MODIS) and solar-induced chlorophyll fluorescence observations from Global Ozone Monitoring Experiment – 2 (GOME-2) (Joiner et al., 2013). Joiner et al. (2018) show that the agreement between FLUXSAT-GPP and GPP from flux towers is better than other available upscaled GPP products.

2.5.2 Evaluation against aircraft CO_2 observations

The aircraft observations used in this study include those published in ObsPack August 2019 (CarbonTracker team, 2019), which include regular vertical profiles from flask samples collected on light aircraft by NOAA (Sweeney et al., 2015) and other laboratories, aircraft campaigns from Atmospheric Tomography (ATom, Wofsy et al., 2018) and HIAPER Pole-to-Pole (HIPPO, Wofsy et al., 2011), regular (two to four weekly) vertical profiles from the Instituto de Pesquisas Espaciais (INPE) over tropical South America (SA) (Gatti et al., 2014), and the O_2/N_2 Ratio and CO_2 airborne Southern Ocean (ORCAS) Study aircraft campaign (Stephens et al., 2017) (Table 3). Figure 2 shows the aircraft observation coverage and density between 2010 and 2018. Most of the aircraft observations are concentrated over NA. ATom had four (1–4) campaigns between August 2016 to May 2018, spanning four seasons over the Pacific and Atlantic Ocean. HIPPO had five (1–5) campaigns over Pacific, and only HIPPO 3–5 occurred between 2010 and 2011. HIPPO 1–2 occurred in 2009. Based on the spatial distribution of aircraft observations, we divide the comparison into nine regions: Alaska, mid-latitude NA, Europe, East Asia, South Asia, Africa, Australia, Southern Ocean, and South America (Table 4 and Figure 2).

https://doi.org/10.5194/essd-2020-123
Preprint. Discussion started: 7 July 2020

We calculate several quantities to evaluate the posterior fluxes and its uncertainty with aircraft observations. One is the monthly mean differences between posterior and aircraft CO_2 mole fractions. The second is the monthly root mean square errors (RMSE) over each nine sub-regions, which is defined as:

$$RMSE = \left(\frac{1}{n}\sum_{i=1}^{n}(y^{o}_{aircraft} - y^{b}_{aircraft})_i^2\right)^{\frac{1}{2}} \quad (2)$$

where $y^{o}_{aircraft}$ is i^{th} aircraft observation, $y^{b}_{aircraft}$ is the corresponding posterior CO_2 mole fractions sampled at i^{th} aircraft locations, and n is the number of aircraft observations over each region. The RMSE is computed over the n aircraft observations within one of the nine sub-regions. The mean differences indicate the magnitude of mean posterior CO_2 bias, while the RMSE includes both random and systematic errors in posterior CO_2. The bias and RMSE could be due to errors in either posterior fluxes or transport or both. When transport errors are smaller than errors in posterior fluxes, the magnitude of biases and *RMSE* indicates the accuracy of posterior fluxes.

To evaluate the magnitude of posterior flux uncertainty estimates, we compare *RMSE* against the standard deviation of ensemble simulated aircraft observations (equation 3) from the Monte Carlo method ($RMSE_{MC}$). The quantity $RMSE_{MC}$ can be written as:

$$RMSE_{MC} = \left[\frac{1}{nens}\sum_{iens=1}^{nens}\left((y^{b(MC)}_{aircraft})_{iens} - \bar{y}^{b(MC)}_{aircraft}\right)^2\right]^{\frac{1}{2}} \quad (3)$$

The variable $(y^{b(MC)}_{aircraft})_{iens}$ is the i^{th} ensemble member of simulated aircraft observations from Monte Carlo ensemble simulations, $\bar{y}^{b(MC)}_{aircraft}$ is the mean, and *nens* is the total number of ensemble members. For simplicity, in equation (3), we drop the indices for the aircraft observations used in equation (2). In the absence of transport errors, when the estimated posterior flux uncertainty reflects the "*true*" posterior flux uncertainty, we show in the *Appendix* that:

https://doi.org/10.5194/essd-2020-123
Preprint. Discussion started: 7 July 2020

$$RMSE^2 = R_{aircraft} + {RMSE_{MC}}^2 \qquad (4)$$

where $R_{aircraft}$ is the aircraft observation error variance, which could be neglected on regional scales. We further calculate the ratio *r* between *RMSE* and $RMSE_{MC}$:

$$r = \frac{RMSE}{RMSE_{MC}} \qquad (5)$$

A ratio close to one indicates that the posterior flux uncertainty reflects the true uncertainty in the posterior fluxes when the transport errors are small.

The presence of transport errors will make the comparison between *RMSE* and $RMSE_{MC}$ potentially difficult to interpret. Even when $RMSE_{MC}$ represents the actual uncertainty in posterior fluxes, the *RMSE* could be larger than $RMSE_{MC}$, since the differences between aircraft observations and model simulated posterior mole fractions *RMSE* could be due to errors in both transport and the posterior fluxes, while $RMSE_{MC}$ only reflects the impact of posterior flux uncertainty on simulated aircraft observations. In this study, we assume the primary sources of *RMSE* come from errors in posterior fluxes.

The *RMSE* and $RMSE_{MC}$ comparison only shows differences in CO_2 space. We further calculate the sensitivity of *RMSE* to posterior flux using GEOS-Chem adjoint. We first define a cost function *J* as:

$$J = RMSE^2 \qquad (6)$$

The sensitivity of the mean-square error to a flux, *x*, at location *i* and month *j* is

$$w_{i,j} = \frac{\partial J}{\partial x_{i,j}} \times x_{i,j} \quad (7)$$

https://doi.org/10.5194/essd-2020-123
Preprint. Discussion started: 7 July 2020

This sensitivity is normalized by the flux magnitude. Equation 7 can be interpreted as the sensitivity of the $RMSE^2$ to a fractional change in the fluxes. We can estimate the time-integrated magnitude of the sensitivity over the entire assimilation window by calculating:

$$S_i = \frac{\sum_{j=1}^{M}|w_{i,j}|}{\sum_{k=1}^{P}\sum_{j=1}^{M}|w_{k,j}|} \quad (8)$$

where P is the total number of grid points and M is the total number of months from the time of the aircraft data to the beginning of the inversion. The numerator of equation (8) quantifies the absolute total sensitivity of the $RMSE^2$ to the fluxes at the i^{th} grid. Normalized by the total absolute sensitivity across the globe, the quantity S_i indicates the relative sensitivity of $RMSE^2$ to fluxes at the i^{th} grid point. Note that S_i is unitless, and it only quantifies sensitivity, not the contribution of fluxes at each grid to $RMSE^2$.

2.6 Regional masks

We provide posterior NBE from 2010 – 2018 using two sets of aggregated regions, for a few selected FLUXNET tower sites, and the underlying gridded product. The regional mask in Figure 3A is based on a combination of seven plant function types condensed from MODIS IGBP and the TRANSCOM -3 region mask (Gurney et al., 2004). There are 28 regions in Figure 3A: six in NA, four in SA, five in Eurasia (north of 40°N), three in tropical Asia, three in Australia, and seven in Africa. The regional mask in Figure 3B is based on latitude and continents, and there are 13 regions in total.

3 Dataset description

We present the gridded fluxes as globally, latitudinally, and regionally time series. We show the nine-year average fluxes aggregated into 28 and 13 geographic regions (Figure 3). The

https://doi.org/10.5194/essd-2020-123
Preprint. Discussion started: 7 July 2020

aggregations are geographic (latitude and continent), bio-climatic (biome by continent), and flux-oriented (for a set of selected flux sites). For each region in the geographic and biome aggregations, we show nine-year mean annual net fluxes and uncertainties, and then the annual fluxes for each region as a set of time-series plots. The month-by-month fluxes and uncertainties are available in tabular format, so the actual aggregated fluxes may be readily compared to bottom-up extrapolated fluxes and Earth System models. Users can also aggregate the gridded fluxes and uncertainties based on their own defined regional masks. Table 5 provides a complete list of all data products available in the dataset. In section 4, we describe the major characteristics of the dataset.

4 Characteristics of the dataset

4.1 Global fluxes

The annual atmospheric CO_2 growth rate, which is the sum of fossil fuel emissions and total annual sink over land and ocean, is well-observed by NOAA surface CO_2 observing network (https://www.esrl.noaa.gov/gmd/ccgg/ggrn.php) (Freidlingstein et al., 2019). We compare the global total flux estimates constrained by GOSAT and OCO-2 with the NOAA CO_2 growth rate from 2010–2018, and discuss the mean carbon sink over land and ocean. Over these nine years, the satellite-constrained atmospheric CO_2 growth rate agrees with the NOAA observed CO_2 growth rate within the uncertainty of posterior fluxes (Figure 4). The mean annual global surface CO_2 flux (in Gt C/yr) is derived from the NOAA observed CO_2 growth rate (in ppm/yr) using a conversion factor of 2.124 GtC/ppm (Le Quéré et al., 2018). The estimated growth rate has the largest discrepancy with the NOAA observed growth rate in 2014, which may be due to a failure of one of the two solar paddles in May 2014 (Kuze et al., 2016). Over the nine years, the estimated total accumulated carbon in the atmosphere is 41.5 ± 2.4 GtC, which is slightly lower than the accumulated carbon based on NOAA CO_2 growth rate (45.2 ± 0.4 GtC). On average, the land sink is 20 ± 8% of fossil

https://doi.org/10.5194/essd-2020-123
Preprint. Discussion started: 7 July 2020

fuel emissions, and the ocean sink is 30 ± 1% of fossil fuel emissions (Figure 4). These numbers are within the ranges of the corresponding estimates from GCP 2019 (Freidlingstein et al., 2019). The mean NBE and ocean sink from GCP 2019 are 21 ± 10% (~1.0 GtC estimated residual NBE uncertainty) and 26 ± 5% (~0.5 GtC estimated ocean flux uncertainty) of fossil fuel emissions respectively between 2010–2018. The GCP NBE here is calculate as the residual differences between fossil fuel, ocean fluxes, and atmospheric CO_2 growth rate, and it is also equivalent to the sum of carbon fluxes from land use changes, land sink, and residual balance reported by GCP. Over these nine years, we estimate that the land sink ranges from 37% of fossil fuel emissions in 2011 (a La Niña year) to only 5% in 2015 (an El Niño year), consistent with GCP estimated range of 35% in 2011 to 7% in 2015. We estimate that the ocean sinks range from 39% in 2015 to 23% of fossil fuel emissions in 2012, larger than the GCP estimated ocean flux ranges of 25% to 28% of fossil fuel emissions (Freidlingstein et al., 2019).

4.2 Mean regional fluxes and uncertainties

Figure 5 shows the nine-year mean regional annual fluxes, uncertainty, and its variability between 2010–2018. Table 6 shows an example of the dataset corresponding to Figure 5 A, C, and E. It shows large net carbon uptake occurs over Eurasia, NA, and Southern Hemisphere (SH) mid-latitudes. The largest net carbon uptake is over eastern US (-0.4 ± 0.1 GtC (1σ uncertainty)) and high latitude Eurasia (-0.4 ± 0.1 GtC) (Figure 5A, B). We estimate a net land carbon sink of 2.5 ± 0.3 GtC/year between 2010–2013 over the NH mid to high latitudes, which agrees with 2.4 ± 0.6 GtC estimates over the same time periods based on a two-box model (Ciais et al., 2019). Net uptake in the tropics ranges from close-to-neutral in tropical South America (0.0 ± 0.1 GtC) to a net source in northern Africa (0.6 ± 0.2 GtC) (Figure 5A, B). The tropics exhibit both large uncertainty and large variability. The NBE interannual variability over northern Africa and tropical SA are 0.5 GtC

https://doi.org/10.5194/essd-2020-123
Preprint. Discussion started: 7 July 2020

and 0.3 GtC respectively, larger than the 0.2 GtC and 0.1 GtC uncertainty (Figure 5C, D). We also find collocation of regions with large NBE and GPP interannual variability (Figure S4).

4.3 Interannual variabilities and uncertainties

Here we present hemispheric and regional NBE interannual variabilities and corresponding uncertainties (Figures 6 and 7, and corresponding tabular data files). In Figure 6, we further divide the globe into three large latitude bands: tropics (20°S–20°N), NH extra-tropics (20°N–85°N), and SH extra-tropics (60°S–20°S). The tropical NBE contributes 90% to the global NBE interannual variability (IAV). The IAV of NBE over the extra-tropics is only about one-third of that over the tropics. The dominant role of tropical NBE in the global IAV of NBE agrees with Figure 4 in Sellers et al. (2018). The top-down global annual NBE anomaly is within the 1.0 GtC/yr uncertainty of residual NBE (i.e., fossil fuel – atmospheric growth – ocean sink) calculated from GCP-2019 (Friedlinston et al., 2019) (Figure 6).

Figure 7 shows the annual NBE anomalies and uncertainties over a few selected regions. Positive NBE indicates reduced net uptake relative to the 2010–2018 mean, and vice versa. Also shown in Figure 7 are GPP anomalies estimated from FLUXSAT. Positive GPP indicates increased productivity, and vice versa. GPP drives NBE in years where anomalies are inversely correlated (e.g., positive NBE and negative GPP), and TER drives NBE in years where anomalies of GPP and NBE have the same sign or weakly correlated. Over tropical SA evergreen broadleaf forest, the largest positive NBE anomalies occur during 2015–2016 El Niño, corresponding to large reductions in productively, consistent with Liu et al. (2017). In 2017, the region sees increased net uptake and increased productivity, implying a recovery from the 2015–2016 El Niño event. The

https://doi.org/10.5194/essd-2020-123
Preprint. Discussion started: 7 July 2020

variability in GPP explains 80% of NBE variability over this region over the nine-year period. In Australian shrubland, our inversion captures the increased net uptake in 2010 and 2011 due to increased precipitation (Pouter et al., 2014) and increased productivity. The variability in GPP explains 70% of the interannual variability in NBE. Over tropical south America Savanna, the NBE interannual variability also shows strong negative correlations with GPP, with GPP explaining 40% of NBE interannual variability. Over the mid-latitude regions where the IAV is small, the R^2 between GPP and NBE is also small (0.0–0.5) as expected. But the increased net uptake generally corresponds to increased productivity. We also do not expect perfect negative correlation between NBE anomalies and GPP anomalies, as discussed in section 2.5. The comparison between NBE and GPP provides insight into when and where net fluxes are likely dominated by productivity.

4.4 Seasonal cycle

We provide a top-down CO_2 constrained regional mean NBE seasonal cycle and its variability and uncertainty. The seasonal cycle of NBE, including its phase (i.e., transition from source to sink) and amplitude (peak-to-trough difference), have large uncertainties, not only over the less-observed tropical regions, but also over the extra-tropics (e.g., Yang et al., 2007; Keppel-Aleks et al., 2012). Figure 8 shows NBE and GPP seasonal cycles for six selected regions. In general, the months that have larger productivity corresponds to months with a net uptake of carbon from the atmosphere. The NH mid-to-high latitudes have larger seasonal cycle amplitudes (Figure 8A, B) compared to the other regions, and their NBE seasonalities are more closely linked to that of GPP (R^2 = 0.9). In the tropics, the relationship between NBE and GPP seasonality is less clear partially

https://doi.org/10.5194/essd-2020-123
Preprint. Discussion started: 7 July 2020

due to the weak seasonality of NBE (Figure 8E, F). The variability and uncertainty of monthly mean fluxes are larger over the tropics and the SH extratropics than over the NH extratropics.

5 Evaluation against independent aircraft CO_2 observations

5.1 Comparison to aircraft observations over nine sub-regions

In this section, we evaluate posterior CO_2 against aircraft observations over nine sub-regions listed in Table 4 and Figure 2. We compare the posterior to aircraft CO_2 mole fractions above planetary boundary layer and up to mid troposphere (1–5 km) at the locations and time of aircraft observations, and then calculate the monthly mean error statistics between 1–5 km. The aircraft observations between 1–5 km are more sensitive to regional fluxes (Liu et al., 2015; Liu and Bowman, 2016). Scatter plots in the left column of Figure 9 show regional monthly mean detrended aircraft CO_2 observations (x-axis) versus the simulated detrended posterior CO_2 (y-axis). We used NOAA global CO_2 trend to detrend both the observations and model simulated mole fractions (ftp://aftp.cmdl.noaa.gov/products/trends/co2/co2_trend_gl.txt). Over the NH regions (A, B, C, D) and Africa (F), the R^2 is equal or above 0.9, which indicates that the posterior CO_2 captures the observed seasonality. The low R^2 (0.7) value in South Asia is caused by one outlier. Over Southern Ocean, Australia, and SA, the R^2 is between 0.2 and 0.4, reflecting weaker CO_2 seasonality over these regions.

The right panel of Figure 9 shows the monthly mean differences between posterior CO_2 and aircraft observations (black), the number of aircraft observations (blue bar, right y-axis), *RMSE* (equation 2) (blue line), and $RMSE_{MC}$ (equation 3) (red line). The magnitude of mean differences between posterior CO_2 and aircraft observations is less than 0.5 ppm except over Southern Ocean, which has a -0.8 ppm bias. The mean differences between posterior CO_2 and aircraft observations are

https://doi.org/10.5194/essd-2020-123
Preprint. Discussion started: 7 July 2020

primarily caused by errors in transport and biases in assimilated satellite observations, while $RMSE_{MC}$ is 'internal flux error' projected into mole fraction space. With the exception of the Southern Ocean, for all regions mean bias is significantly less than $RMSE_{MC}$, which suggests that transport and data bias in satellite observations may be much smaller than the internal flux errors.

As demonstrated in section 2.5, comparing *RMSE* and $RMSE_{MC}$ is a test of the accuracy of posterior flux uncertainty estimate. Over all the regions, the differences between *RMSE* and $RMSE_{MC}$ are smaller than 0.3 ppm, which indicates a comparable magnitude between empirical posterior flux uncertainty estimates from Monte Carlo method and the actual posterior flux uncertainty over the regions that these aircraft observations are sensitive to. These aircraft observations are sensitive to fluxes over a broad region as shown in Figure S5.

5.2 Comparison to aircraft observations from ATom and HIPPO aircraft campaigns

Figures 10 and 11 show comparisons to aircraft CO_2 from ATom 1–4 campaigns spanning four seasons, and HIPPO 3–5 over the Pacific Ocean between 1–5 km. The vertical curtain comparisons are shown in Figure S6 and S7. The mean differences between posterior CO_2 and aircraft CO_2 are quite uniform (within 0.5 ppm) throughout the column except over the Atlantic Ocean during ATom 1–2 and the Southern Ocean during ATom 1 (Figures S6 and S7). Also shown in Figures 10 and 11 are *RMSE* of each aircraft campaign (middle column) and the ratio between *RMSE* and $RMSE_{MC}$ (right column). A ratio larger than one between *RMSE* and $RMSE_{MC}$ indicates errors in either transport or low of posterior flux uncertainty estimates (section 2.5).

https://doi.org/10.5194/essd-2020-123
Preprint. Discussion started: 7 July 2020

Over most of flight tracks during ATom 1–4, the posterior CO_2 errors are between -0.5 and 0.5 ppm, the *RMSE* is smaller than 0.5 ppm, and the ratio between *RMSE* and $RMSE_{MC}$ is smaller than or equal to 1. However, off the coast of Africa during ATOM -1 and -2 and over Southern Ocean during ATOM-1, the mean differences between posterior CO_2 and aircraft observations are larger than 0.5 ppm. During ATOM-1 (29 July – 23 Aug 2016), the mean differences between posterior CO_2 and aircraft CO_2 show large negative biases, while during ATOM-2 (26 Jan 2017–21 Feb 2017), it has large positive biases off the coast of Africa. The ratio between *RMSE* and $RMSE_{MC}$ is significantly larger than one over these regions, which indicates an underestimation of posterior flux uncertainty or large magnitude of transport errors during that time period.

We further run adjoint sensitivity analyses over the three regions with ratios significantly larger than one to identify the posterior fluxes that could contribute to the large differences between posterior CO_2 and aircraft observations during ATOM 1–2. We run the adjoint model backward for three months from the observation time and calculate S_i defined in equation (7). Adjoint sensitivity analysis indicates that the large mismatch between aircraft observations and model simulations during ATOM-1 and -2 off the coast of Africa could be potentially driven by errors in posterior fluxes over tropical Africa (Figure S8). These large posterior CO_2 errors and large ratio over Southern Ocean during ATOM-1 are driven by flux errors in oceanic fluxes around 30°S and over Australia (Figure S9).

During the HIPPO aircraft campaigns, the absolute errors in posterior CO_2 across Pacific are less than 0.5 ppm except over the Arctic Ocean and over Alaska in summer (Figure 11), consistent with Figure 10A. The large errors over the Arctic Ocean may be related to both transport errors

https://doi.org/10.5194/essd-2020-123
Preprint. Discussion started: 7 July 2020

and the accuracy of high latitude fluxes. Byrne et al. (2020) provide a brief summary of these challenges in simulating CO_2 over high latitudes with 4° x 5° resolution transport model. Increasing the resolution of the transport model may reduce transport errors over high latitudes.

We run adjoint sensitivity analysis over the high-latitude regions where the differences between posterior CO_2 and aircraft observations are large (Figure 11). The adjoint sensitivity analysis (Figure S10) shows that the large errors over these regions could be driven by errors in fluxes over Alaska as well as broad NH mid-latitude regions.

6 Discussion

Evaluation of posterior flux uncertainty estimates by comparing posterior CO_2 error statistics (*RMSE,* Equation 2) with the standard deviation of ensemble simulated CO_2 from Monte Carlo uncertainty quantification method ($RMSE_{MC}$, equation 3) has its limitations. When *RMSE* and $RMSE_{MC}$ are similar in magnitude, this indicates small magnitude of transport errors and reasonable posterior uncertainty estimates. A much larger *RMSE* than $RMSE_{MC}$ could be due to errors in either transport or underestimation of posterior flux uncertainty or both. The presence of transport errors makes the interpretation of the *RMSE* and $RMSE_{MC}$ complex. A better, independent quantification of transport errors is needed in the future in order to rigorously use the comparison statistics between aircraft observations and posterior CO_2 to diagnose flux errors.

Comparison to aircraft observations shows regionally-dependent accuracy in posterior fluxes. ATom observations show seasonally-dependent biases over the Atlantic, implying possible seasonally dependent errors in posterior fluxes over northern to central Africa. Therefore, we recommend combining NBE with other ancillary variables, e.g., GPP, to better understand carbon

https://doi.org/10.5194/essd-2020-123
Preprint. Discussion started: 7 July 2020

dynamics. Combining NBE with component carbon fluxes can shed light on the processes controlling the changes of NBE (e.g., Bowman et al, 2017; Liu et al., 2017). NBE can be written as:

NBE= TER + fire - GPP (8)

where TER is total ecosystem respiration (TER) (Figure 1). Satellite carbon monoxide (CO) observations provide constraints on fire emissions (Arellano et al, 2006, van der Werf, 2008; Jones et al, 2009; Jiang et al., 2015, Bowman et al, 2017; Liu et al., 2017). In addition to FLUXSAT-GPP product used here, solar induced chlorophyll fluorescence (SIF) can be directly used as a proxy for GPP (e.g., Parazoo et al, 2014). Once NBE, fire, and GPP carbon fluxes are quantified, TER can be calculated as a residual (e.g., Bowman et al, 2017; Liu et al., 2017, 2018).

Because of the diffusive manner of atmospheric transport and the limited observation coverage, the gridded flux values are not independent from each other. The errors and relative uncertainties of the fluxes at each individual grid point are larger than regional aggregated fluxes. For the same reason, comparing NBE with flux tower observations needs caution, though we provide NBE at a few flux tower sites.

The variability and changes are more robust than the mean NBE fluxes from top-down flux inversions in general (Baker et al., 2006b). The errors in transport and potential biases in observations are mostly stable in time, so biases in the mean fluxes tend to cancel out when computing interannual variability and year-to-year changes (Schuh et al., 2019; Crowell et al., 2019).

https://doi.org/10.5194/essd-2020-123
Preprint. Discussion started: 7 July 2020

The global fossil fuel emissions have ~5% uncertainty (GCP, 2019). However, they are regionally inhomogeneous. We neglect the uncertainties in fossil fuel emissions, which will introduce additional error in regions of rapid fossil fuel growth or in areas with noisier statistics (Yin et al., 2019). In the future, we will account for uncertainties in fossil fuel emissions.

The posterior NBE includes all types of land fluxes except fossil fuel emissions, which is equivalent to the sum of land use change fluxes and land sinks published by GCP. The sum of regional NBE and fossil fuel emissions is an index of the contribution of any specific region to the changes of atmospheric CO_2 growth rate. Even over the continental US, where fossil fuel emissions are ~1.5 GtC/year, the changes of regional NBE can significantly modify contributions to the changes of atmospheric CO_2 (Liu et al., 2018). Since NBE has high variability and its predicted changes in the future are likely to have large uncertainties, quantifying regional NBE is critical to monitoring regional contributions to atmospheric CO_2 growth rate, and ultimately to guide mitigation to limit warming to 1.5°C above pre-industrial level (IPCC, AR6).

7 Summary

Terrestrial biosphere carbon fluxes are the largest contributor to the interannual variability of the atmospheric CO_2 growth rate. Therefore, monitoring its change at regional scales is essential for understanding how it responds to CO_2, climate and land use. Here, we present the longest terrestrial flux estimates and their uncertainties constrained by X_{CO2} from 2010–2018 on self-consistent global and regional scales (CMS-Flux NBE 2020). We qualitatively evaluate the net flux estimates by comparing its variability with GPP variability, and provide comprehensive evaluation of posterior fluxes and the uncertainties by comparing posterior CO_2 with independent aircraft CO_2.

https://doi.org/10.5194/essd-2020-123
Preprint. Discussion started: 7 July 2020

The estimated posterior flux uncertainty agrees with the expected uncertainty in the posterior fluxes based on the comparison to aircraft CO_2 observations. This dataset can be used in understanding controls on regional NBE interannual variability, evaluating biogeochemical models, and provide support the monitoring of the regional contributions to the changes in atmospheric CO_2.

8 Data availability and future update

The CMS-Flux NBE 2020 data is available at: https://doi.org/10.25966/4v02-c391 (Liu et al., 2020). The regional aggregated fluxes are provided as *csv* files with file size ~10MB, and the gridded data is provided in NetCDF format with file size ~10MB. The full ensemble posterior fluxes used to estimate posterior flux uncertainties are provided in NetCDF format with file size ~20MB. Table 7 lists the sources of the data used in producing and evaluating the CMS-Flux NBE 2020 data product.

The quality of X_{CO2} from satellite observations is continually improving. The OCO-2 v10 X_{CO2} will be released in June 2020, and the full GOSAT record (June 2009–Jan 2020) processed by the same retrieval algorithm as OCO-2 will be released around the same time. Continuing to improving the quality of satellite observations and extending the NBE estimates beyond 2018 in the future will help us better understand interactions between terrestrial biosphere carbon cycle and climate and provide support in monitoring the regional contributions to the changes of atmospheric CO_2. Thus, we plan a future update of the dataset on an annual basis, with a goal to support current scientific research and policy making.

9 Author contributions

JL designed the study and led the writing of the paper in close collaboration with KB and DS. LB helped generate the plots and created all the data files. AAB provided the prior of the terrestrial biosphere carbon fluxes. NP helped interpret the GPP evaluation. DM and DC generated the prior ocean carbon fluxes. TO generated the ODIAC fossil fuel emissions. JJ provided the FLUXSAT GPP product. BD and SW provided and contributed to the interpretation of HIPPO aircraft CO_2 observation comparisons. BS, KM, and CS provided ORCAS aircraft CO_2 observations and contributed interpretation of aircraft CO_2 observation comparisons. LVG and JM provided INPE aircraft CO_2 observations and contributed interpretation of aircraft CO_2 observation comparisons. CS and KM provided ATom and NOAA aircraft CO2 observations and contributed interpretation of aircraft CO_2 observation comparisons. We furthermore acknowledge funding from the EU for the ERC project "ASICA" (grant number 649087) to Wouter Peters (Groningen University) and EU and NERC (UK) funding to Emanuel Gloor (University of Leeds), which contributed to the INPE Amazon greenhouse sampling program. All authors contributed to the writing, and have reviewed and approved the paper.

10 Competing interest

The authors declare that they have no conflict of interest.

Acknowledgement

Resources supporting this work were provided by the NASA High-End Computing (HEC) Program through the NASA Advanced Supercomputing (NAS) division at Ames Research Center. We acknowledge the funding support from NASA OCO-2/3 Science Team, Carbon Monitoring System (CMS), and Making Earth Science Data Records for Use in Research Environments (MEaSUREs) programs. Tomohiro Oda is supported by the NASA Carbon Cycle Science program (grant no. NNX14AM76G). We acknowledge EU and NERC (UK) funding to Emanuel

https://doi.org/10.5194/essd-2020-123
Preprint. Discussion started: 7 July 2020

Gloor, University of Leeds which substantially contributed to the INPE Amazon greenhouse sampling program. Part of the research was carried out at Jet Propulsion Laboratory, Caltech.

Appendix

As shown in Kalnay (2003):

$RMSE^2 = R_{aircraft} + HP^aH^T$ (A.1)

where $R_{aircraft}$ is the aircraft observation error variance, and P^a is the posterior flux error covariance. The H is linearized observation operator, which transfers posterior flux errors to aircraft observation space, and H^T is its adjoint. In the Monte Carlo method, the postieror flux error covariance P^a is approximated by:

$P^a = \frac{1}{nens} X^a X^{a^T}$ (A.2)

where X^a is the ensemble perturbations written as:

$X^a = x^a - \bar{x}^a$ (A.3)

where x^a is the ensemble posterior fluxes from Monte Carlo, and $\bar{x}^a$ is the mean.

Therefore, HP^aH^T can be written as:

$HP^aH^T = \frac{1}{nens}[h(x^a) - h(\bar{x}^a)][h(x^a) - h(\bar{x}^a)]^T$ (A.4)

The right hand side is the same as the definiation of $RMSE_{MC}$ in the main text.

Therefore, when the posterior flux uncertainty estimated by Monte Carlo method represents the actual uncertainty in posterior fluxes, equation (A.1) can be written as:

$RMSE^2 = R_{aircraft} + RMSE_{MC}^2$ (A.5).

It is the same as equation (3) in the main text.

References

Arellano Jr, A.F., Kasibhatla, P.S., Giglio, L., Van der Werf, G.R., Randerson, J.T., and Collatz, G.J.: Time-dependent inversion estimates of global biomass-burning CO emissions using Measurement of Pollution in the Troposphere (MOPITT) measurements, J. Geophys. Res: Atmos., 111, D09303, https://doi.org/10.1029/2005JD006613, 2006.

Baker, D.F., Doney, S.C., and Schimel, D.S.: Variational data assimilation for atmospheric CO2, Tellus B: Chem. Phys. Meteorol., 58, 359-365, https://doi.org/10.1111/j.1600-0889.2006.00218.x, 2006a.

Baker, D.F., Law, R.M., Gurney, K.R., Rayner, P., Peylin, P., Denning, A.S., Bousquet, P., Bruhwiler, L., Chen, Y.H., Ciais, P., and Fung, I.Y.: TransCom 3 inversion intercomparison: Impact of transport model errors on the interannual variability of regional CO2 fluxes, 1988–2003, Global Biogeochem. Cy., 20, GB1002, https://doi.org/10.1029/2004GB002439, 2006b.

Bastos, A., Friedlingstein, P., Sitch, S., Chen, C., Mialon, A., Wigneron, J.-P., Arora, V. K., Briggs, P. R., Canadell, J. G., and Ciais, P.: Impact of the 2015/2016 El Niño on the terrestrial carbon cycle constrained by bottom-up and top-down approaches. Philos. Trans. R Soc. Lond. B. Biol. Sci., 373, 1760, https://doi.org/10.1098/rstb.2017.0304, 2018.

Bloom, A.A., Exbrayat, J.F., van der Velde, I.R., Feng, L., and Williams, M.: The decadal state of the terrestrial carbon cycle: Global retrievals of terrestrial carbon allocation, pools, and residence times. Proc. Natl Acad. Sci., 113, 1285-1290, 2016.

Bloom, A. A., Bowman, K. W., Liu, J., Konings, A. G., Worden, J. R., Parazoo, N. C., Meyer, V., Reager, J. T., Worden, H. M., Jiang, Z., Quetin, G. R., Smallman, T. L., Exbrayat, J.-F., Yin, Y., Saatchi, S. S., Williams, M., and Schimel, D. S.: Lagged effects dominate the inter-annual variability of the 2010–2015 tropical carbon balance, Biogeosciences Discuss., https://doi.org/10.5194/bg-2019-459, in review, 2020.

Bowman, K.W., Liu, J., Bloom, A.A., Parazoo, N.C., Lee, M., Jiang, Z., Menemenlis, D., Gierach, M.M., Collatz, G.J., Gurney, K.R., and Wunch, D.: Global and Brazilian carbon response to El Niño Modoki 2011–2010, Earth Space Sci., 4, 637-660, https://doi.org/10.1002/2016EA000204, 2017.

Brix, H., Menemenlis, D., Hill, C., Dutkiewicz, S., Jahn, O., Wang, D., Bowman, K., and Zhang, H.: Using Green's Functions to initialize and adjust a global, eddying ocean biogeochemistry general circulation model, Ocean Model., 95, 1-14, https://doi.org/10.1016/j.ocemod.2015.07.008, 2015.

Byrd, R.H., Nocedal, J., and Schnabel, R.B.: Representations of quasi-Newton matrices and their use in limited memory methods, Math. Program., 63, 129-156, https://doi.org/10.1007/BF01582063, 1994.

https://doi.org/10.5194/essd-2020-123
Preprint. Discussion started: 7 July 2020

Byrne, B., Liu, J., et al.: Improved constraints on northern extratropical CO2 fluxes obtained by combining surface-based and space-based atmospheric CO2 measurements, *JGR-Atmosphere*, (*minor revision*), 2020

Carroll, D., Menemenlis, D., Adkins, J.: The ECCO-Darwin Data-assimilative Global Ocean Biogeochemistry Model: Estimates of Seasonal to Multi-decadal Surface Ocean pCO2 and Air-sea CO2 Flux. *Journal of Advances in Modeling Earth Systems* (*minor revision*), 2020

Chevallier, F., Fisher, M., Peylin, P., Serrar, S., Bousquet, P., Bréon, F.M., Chédin, A., and Ciais, P.: Inferring CO2 sources and sinks from satellite observations: Method and application to TOVS data, J. Geophys. Res.-Atmos., 110, D24309, https://doi.org/10.1029/2005JD006390, 2005.

Chevallier, F., Ciais, P., Conway, T.J., Aalto, T., Anderson, B.E., Bousquet, P., Brunke, E.G., Ciattaglia, L., Esaki, Y., Fröhlich, M., and Gomez, A.: CO_2 surface fluxes at grid point scale estimated from a global 21 year reanalysis of atmospheric measurements, J. Geophys. Res., 115, D21307, https://doi.org/10.1029/2010JD013887, 2010.

Chevallier, F., Remaud, M., O'Dell, C. W., Baker, D., Peylin, P., and Cozic, A.: Objective evaluation of surface- and satellite-driven carbon dioxide atmospheric inversions, Atmos. Chem. Phys., 19, 14233–14251, https://doi.org/10.5194/acp-19-14233-2019, 2019.

Ciais, P., Tan, J., Wang, X., Roedenbeck, C., Chevallier, F., Piao, S.L., Moriarty, R., Broquet, G., Le Quéré, C., Canadell, J.G., and Peng, S.: Five decades of northern land carbon uptake revealed by the interhemispheric CO 2 gradient, Nature, 568, 221-225, https://doi.org/10.1038/s41586-019-1078-6, 2019.

Crisp, D., Fisher, B. M., O'Dell, C., Frankenberg, C., Basilio, R., Bösch, H., Brown, L. R., Castano, R., Connor, B., Deutscher, N. M., Eldering, A., Griffith, D., Gunson, M., Kuze, A., Mandrake, L., McDuffie, J., Messerschmidt, J., Miller, C. E., Morino, I., Natraj, V., Notholt, J., O'Brien, D. M., Oyafuso, F., Polonsky, I., Robinson, J., Salawitch, R., Sherlock, V., Smyth, M., Suto, H., Taylor, T. E., Thompson, D. R., Wennberg, P. O., Wunch, D., and Yung, Y. L.: The ACOS CO_2 retrieval algorithm – Part II: Global X_{CO2} data characterization, Atmos. Meas. Tech., 5, 687–707, https://doi.org/10.5194/amt-5-687-2012, 2012.

Crisp, D., Pollock, H. R., Rosenberg, R., Chapsky, L., Lee, R. A. M., Oyafuso, F. A., Frankenberg, C., O'Dell, C. W., Bruegge, C. J., Doran, G. B., Eldering, A., Fisher, B. M., Fu, D., Gunson, M. R., Mandrake, L., Osterman, G. B., Schwandner, F. M., Sun, K., Taylor, T. E., Wennberg, P. O., and Wunch, D.: The on-orbit performance of the Orbiting Carbon Observatory-2 (OCO-2) instrument and its radiometrically calibrated products, Atmos. Meas. Tech., 10, 59–81, https://doi.org/10.5194/amt-10-59-2017, 2017.

Crowell, S., Baker, D., Schuh, A., Basu, S., Jacobson, A. R., Chevallier, F., Liu, J., Deng, F., Feng, L., McKain, K., Chatterjee, A., Miller, J. B., Stephens, B. B., Eldering, A., Crisp, D., Schimel, D., Nassar, R., O'Dell, C. W., Oda, T., Sweeney, C., Palmer, P. I., and Jones, D. B. A.: The 2015–

https://doi.org/10.5194/essd-2020-123
Preprint. Discussion started: 7 July 2020

2016 carbon cycle as seen from OCO-2 and the global in situ network, Atmos. Chem. Phys., 19, 9797–9831, https://doi.org/10.5194/acp-19-9797-2019, 2019.

Falk, M., Wharton, S., Schroeder, M., Ustin, S., and U, K.T.P.: Flux partitioning in an old-growth forest: seasonal and interannual dynamics. Tree Physiol., 28, 509-520, https://doi.org/10.1093/treephys/28.4.509, 2008.

Friedlingstein, P., Meinshausen, M., Arora, V.K., Jones, C.D., Anav, A., Liddicoat, S.K., and Knutti, R.: Uncertainties in CMIP5 climate projections due to carbon cycle feedbacks, J. Clim., 27, 511-526, https://doi.org/10.1175/JCLI-D-12-00579.1, 2014.

Friedlingstein, P., Jones, M., O'Sullivan, M., Andrew, R., Hauck, J., Peters, G., Peters, W., Pongratz, J., Sitch, S., Le Quéré, C., and DBakker, O.: Global carbon budget 2019, Earth Syst. Sci. Data, 11, 1783-1838, https://doi.org/10.3929/ethz-b-000385668, 2019.

Gatti, L.V., Gloor, M., Miller, J.B., Doughty, C.E., Malhi, Y., Domingues, L.G., Basso, L.S., Martinewski, A., Correia, C.S.C., Borges, V.F., and Freitas, S., 2014, Drought sensitivity of Amazonian carbon balance revealed by atmospheric measurements, Nature, 506, 76-80, https://doi.org/10.1038/nature12957, 2014.

Gaubert, B., Stephens, B. B., Basu, S., Chevallier, F., Deng, F., Kort, E. A., Patra, P. K., Peters, W., Rödenbeck, C., Saeki, T., Schimel, D., Van der Laan-Luijkx, I., Wofsy, S., and Yin, Y.: Global atmospheric CO_2 inverse models converging on neutral tropical land exchange, but disagreeing on fossil fuel and atmospheric growth rate, Biogeosciences, 16, 117–134, https://doi.org/10.5194/bg-16-117-2019, 2019.

Gurney, K.R., Law, R.M., Denning, A.S., Rayner, P.J., Pak, B.C., Baker, D., Bousquet, P., Bruhwiler, L., Chen, Y.H., Ciais, P., and Fung, I.Y.: Transcom 3 inversion intercomparison: Model mean results for the estimation of seasonal carbon sources and sinks, Global Biogeochem. Cycles, 18, GB1010, https://doi.org/10.1029/2003GB002111, 2004.

Henze, D. K., Hakami, A., and Seinfeld, J. H.: Development of the adjoint of GEOS-Chem, Atmos. Chem. Phys., 7, 2413–2433, https://doi.org/10.5194/acp-7-2413-2007, 2007.

Jiang, Z., Worden, J. R., Worden, H., Deeter, M., Jones, D. B. A., Arellano, A. F., and Henze, D. K.: A 15-year record of CO emissions constrained by MOPITT CO observations, Atmos. Chem. Phys., 17, 4565–4583, https://doi.org/10.5194/acp-17-4565-2017, 2017.

Joiner, J., Guanter, L., Lindstrot, R., Voigt, M., Vasilkov, A. P., Middleton, E. M., Huemmrich, K. F., Yoshida, Y., and Frankenberg, C.: Global monitoring of terrestrial chlorophyll fluorescence from moderate-spectral-resolution near-infrared satellite measurements: methodology, simulations, and application to GOME-2, Atmos. Meas. Tech., 6, 2803–2823, https://doi.org/10.5194/amt-6-2803-2013, 2013.

https://doi.org/10.5194/essd-2020-123
Preprint. Discussion started: 7 July 2020

Joiner, J., Yoshida, Y., Zhang, Y., Duveiller, G., Jung, M., Lyapustin, A., Wang, Y., & Tucker, C.: Estimation of terrestrial global gross primary production (GPP) with satellite data-driven models and eddy covariance flux data. *Remote Sensing*, **10**(9), 1346. https://doi.org/10.3390/rs10091346. 2018.

Jones, D. B. A., Bowman, K. W., Logan, J. A., Heald, C. L., Liu, J., Luo, M., Worden, J., and Drummond, J.: The zonal structure of tropical O_3 and CO as observed by the Tropospheric Emission Spectrometer in November 2004 – Part 1: Inverse modeling of CO emissions, Atmos. Chem. Phys., 9, 3547–3562, https://*doi*.org/*10.5194*/*acp-9-3547-2009* , 2009.

Keppel-Aleks, G., Wennberg, P. O., Washenfelder, R. A., Wunch, D., Schneider, T., Toon, G. C., Andres, R. J., Blavier, J.-F., Connor, B., Davis, K. J., Desai, A. R., Messerschmidt, J., Notholt, J., Roehl, C. M., Sherlock, V., Stephens, B. B., Vay, S. A., and Wofsy, S. C.: The imprint of surface fluxes and transport on variations in total column carbon dioxide, Biogeosciences, 9, 875–891, https://doi.org/10.5194/bg-9-875-2012, 2012.

Kiel, M., O'Dell, C. W., Fisher, B., Eldering, A., Nassar, R., MacDonald, C. G., and Wennberg, P. O.: How bias correction goes wrong: measurement of X_{CO2} affected by erroneous surface pressure estimates, Atmos. Meas. Tech., 12, 2241–2259, https://doi.org/10.5194/amt-12-2241-2019, 2019.

Konings, A. G., Bloom, A. A., Liu, J., Parazoo, N. C., Schimel, D. S., and Bowman, K. W.: Global satellite-driven estimates of heterotrophic respiration, Biogeosciences, 16, 2269–2284, https://doi.org/10.5194/bg-16-2269-2019, 2019.

Kulawik, S. S., Crowell, S., Baker, D., Liu, J., McKain, K., Sweeney, C., Biraud, S. C., Wofsy, S., O'Dell, C. W., Wennberg, P. O., Wunch, D., Roehl, C. M., Deutscher, N. M., Kiel, M., Griffith, D. W. T., Velazco, V. A., Notholt, J., Warneke, T., Petri, C., De Mazière, M., Sha, M. K., Sussmann, R., Rettinger, M., Pollard, D. F., Morino, I., Uchino, O., Hase, F., Feist, D. G., Roche, S., Strong, K., Kivi, R., Iraci, L., Shiomi, K., Dubey, M. K., Sepulveda, E., Rodriguez, O. E. G., Té, Y., Jeseck, P., Heikkinen, P., Dlugokencky, E. J., Gunson, M. R., Eldering, A., Crisp, D., Fisher, B., and Osterman, G. B.: Characterization of OCO-2 and ACOS-GOSAT biases and errors for CO_2 flux estimates, Atmos. Meas. Tech. Discuss., https://doi.org/10.5194/amt-2019-257, in review, 2019.

Kuze, A., Suto, H., Shiomi, K., Kawakami, S., Tanaka, M., Ueda, Y., Deguchi, A., Yoshida, J., Yamamoto, Y., Kataoka, F., Taylor, T. E., and Buijs, H. L.: Update on GOSAT TANSO-FTS performance, operations, and data products after more than 6 years in space, Atmos. Meas. Tech., 9, 2445–2461, https://doi.org/10.5194/amt-9-2445-2016, 2016.

Le Quéré, C., Andrew, R. M., Friedlingstein, P., Sitch, S., Pongratz, J., Manning, A. C., Korsbakken, J. I., Peters, G. P., Canadell, J. G., Jackson, R. B., Boden, T. A., Tans, P. P., Andrews, O. D., Arora, V. K., Bakker, D. C. E., Barbero, L., Becker, M., Betts, R. A., Bopp, L., Chevallier, F., Chini, L. P., Ciais, P., Cosca, C. E., Cross, J., Currie, K., Gasser, T., Harris, I., Hauck, J., Haverd, V., Houghton, R. A., Hunt, C. W., Hurtt, G., Ilyina, T., Jain, A. K., Kato, E., Kautz, M., Keeling, R. F., Klein Goldewijk, K., Körtzinger, A., Landschützer, P., Lefèvre, N., Lenton, A., Lienert, S., Lima, I., Lombardozzi, D., Metzl, N., Millero, F., Monteiro, P. M. S., Munro, D. R., Nabel, J. E.

https://doi.org/10.5194/essd-2020-123
Preprint. Discussion started: 7 July 2020

Open Access Earth System Science Data Discussions

M. S., Nakaoka, S., Nojiri, Y., Padin, X. A., Peregon, A., Pfeil, B., Pierrot, D., Poulter, B., Rehder, G., Reimer, J., Rödenbeck, C., Schwinger, J., Séférian, R., Skjelvan, I., Stocker, B. D., Tian, H., Tilbrook, B., Tubiello, F. N., van der Laan-Luijkx, I. T., van der Werf, G. R., van Heuven, S., Viovy, N., Vuichard, N., Walker, A. P., Watson, A. J., Wiltshire, A. J., Zaehle, S., and Zhu, D.: Global Carbon Budget 2017, Earth Syst. Sci. Data, 10, 405–448, https://doi.org/10.5194/essd-10-405-2018, 2018.

Liu, J., Baskarran, L., Bowman, K., Schimel, D., Bloom, A. A., Parazoo, N., Oda, T., Carrol, D., Menemenlis, D., Joiner, J., Commane, R., Daube, B., Gatti, L. V., McKain, K., Miller, J., Stephens, B. B., Sweeney, C., & Wofsy, S. (2020). *CMS-Flux NBE 2020* [Data set]. NASA. https://doi.org/10.25966/4V02-C391

Liu, J. and Bowman, K.: A method for independent validation of surface fluxes from atmospheric inversion: Application to CO2, Geophys. Res. Lett., 43, 3502-3508, https://doi.org/10.1002/2016GL067828, 2016.

Liu, J., Bowman, K. W., and Henze, D. K.: Source-receptor relationships of column-average $CO_2$and implications for the impact of observations on flux inversions. *J. Geophys. Res. Atmos.*, 120, 5214– 5236. doi: 10.1002/2014JD022914, 2015

Liu, J., Bowman, K.W., Lee, M., Henze, D.K., Bousserez, N., Brix, H., James Collatz, G., Menemenlis, D., Ott, L., Pawson, S., and Jones, D.: Carbon monitoring system flux estimation and attribution: impact of ACOS-GOSAT XCO2 sampling on the inference of terrestrial biospheric sources and sinks. Tellus B Chem. Phys. Meteorol. B., 66, 22486, http://dx.doi.org/10.3402/tellusb.v66.22486, 2014.

Liu, J., Bowman, K.W., Schimel, D.S., Parazoo, N.C., Jiang, Z., Lee, M., Bloom, A.A., Wunch, D., Frankenberg, C., Sun, Y., and O'Dell, C.W.: Contrasting carbon cycle responses of the tropical continents to the 2015–2016 El Niño. Science, 358, eaam5690, https://doi.org/10.1126/science.aam5690, 2017.

Liu, J., Bowman, K., Parazoo, N.C., Bloom, A.A., Wunch, D., Jiang, Z., Gurney, K.R., and Schimel, D.: Detecting drought impact on terrestrial biosphere carbon fluxes over contiguous US with satellite observations. Environ. Res. Lett., 13, 095003, https://doi.org/10.1088/1748-9326/aad5ef, 2018.

Lovenduski, N.S. and Bonan, G.B.: Reducing uncertainty in projections of terrestrial carbon uptake, Environ. Res. Lett., 12, 044020, https://doi.org/10.1088/1748-9326/aa66b8, 2017.

Nassar, R., Jones, D.B., Suntharalingam, P., Chen, J.M., Andres, R.J., Wecht, K.J., Yantosca, R.M., Kulawik, S.S., Bowman, K.W., Worden, J.R., and Machida, T.: Modeling global atmospheric CO2 with improved emission inventories and CO2 production from the oxidation of other carbon species. Geosci. Model Dev., 3, 689-716, https://doi.org/10.5194/gmd-3-689-2010, 2010.

Oda, T., Maksyutov, S., and Andres, R. J.: The Open-source Data Inventory for Anthropogenic CO_2, version 2016 (ODIAC2016): a global monthly fossil fuel CO_2 gridded emissions data product for tracer transport simulations and surface flux inversions, Earth Syst. Sci. Data, 10, 87–107, https://doi.org/10.5194/essd-10-87-2018, 2018.

O'Dell, C. W., Connor, B., Bösch, H., O'Brien, D., Frankenberg, C., Castano, R., Christi, M., Eldering, D., Fisher, B., Gunson, M., McDuffie, J., Miller, C. E., Natraj, V., Oyafuso, F., Polonsky, I., Smyth, M., Taylor, T., Toon, G. C., Wennberg, P. O., and Wunch, D.: The ACOS CO_2 retrieval algorithm – Part 1: Description and validation against synthetic observations, Atmos. Meas. Tech., 5, 99–121, https://doi.org/10.5194/amt-5-99-2012, 2012.

O'Dell, C., Eldering, A., Wennberg, P.O., Crisp, D., Gunson, M., Fisher, B., Frankenberg, C., Kiel, M., Lindqvist, H., Mandrake, L., and Merrelli, A.: Improved retrievals of carbon dioxide from Orbiting Carbon Observatory-2 with the version 8 ACOS algorithm, Atmos. Meas. Tech., 11, 6539–6576, https://doi.org/10.5194/amt-11-6539-2018, 2018.

Olsen, S.C. and Randerson, J.T.: Differences between surface and column atmospheric CO2 and implications for carbon cycle research, J. Geophys. Res: Atmos., 109, D02301, https://doi.org/10.1029/2003JD003968, 2004.

Parazoo, N.C., Bowman, K., Fisher, J.B., Frankenberg, C., Jones, D.B.A., Cescatti, A., Pérez-Priego, Ó., Wohlfahrt, G. and Montagnani, L.: Terrestrial gross primary production inferred from satellite fluorescence and vegetation models. Glob Change Biol, 20: 3103-3121. doi:10.1111/gcb.12652. 2014.

Poulter, B., Frank, D., Ciais, P., Myneni, R.B., Andela, N., Bi, J., Broquet, G., Canadell, J.G., Chevallier, F., Liu, Y.Y., and Running, S.W.: Contribution of semi-arid ecosystems to interannual variability of the global carbon cycle, Nature, 509, 600-603, https://doi.org/10.1038/nature13376, 2014.

Quetin, G., Bloom, A. A., Bowman, K. W., & Konings, A.: Carbon flux variability from a relatively simple ecosystem model with assimilated data is consistent with terrestrial biosphere model estimates. *Journal of Advances in Modeling Earth Systems*, 12, e2019MS001889. https://doi.org/10.1029/2019MS001889, 2020

Randerson, J.T., Van Der Werf, G.R., Giglio, L., Collatz, G.J., and Kasibhatla, P.S.: Global Fire Emissions Database, Version 4.1 (GFEDv4), ORNL DAAC, Oak Ridge, Tennessee, USA, https://doi.org/10.3334/ORNLDAAC/1293, 2018.

Rienecker, M.M., Suarez, M.J., Gelaro, R., Todling, R., Bacmeister, J., Liu, E., Bosilovich, M.G., Schubert, S.D., Takacs, L., Kim, G.K., and Bloom, S.: MERRA: NASA's modern-era retrospective analysis for research and applications, J. Clim., 24, 3624-3648, https://doi.org/10.1175/JCLI-D-11-00015.1, 2011.

Running, S.W., Baldocchi, D.D., Turner, D.P., Gower, S.T., Bakwin, P.S., and Hibbard, K.A.: A global terrestrial monitoring network integrating tower fluxes, flask sampling, ecosystem

https://doi.org/10.5194/essd-2020-123
Preprint. Discussion started: 7 July 2020

modeling and EOS satellite data, Remote Sens. Environ., 70, 108-127, https://doi.org/10.1016/S0034-4257(99)00061-9, 1999.

Schuh, A.E., Jacobson, A.R., Basu, S., Weir, B., Baker, D., Bowman, K., Chevallier, F., Crowell, S., Davis, K.J., Deng, F., and Denning, S.: Quantifying the impact of atmospheric transport uncertainty on CO2 surface flux estimates, Global Biogeochem. Cy., 33, 484-500, https://doi.org/10.1029/2018GB006086, 2019.

Sellers, P.J., Schimel, D.S., Moore, B., Liu, J., and Eldering, A.: Observing carbon cycle–climate feedbacks from space, PNAS, 115, 7860-7868, https://doi.org/10.1073/pnas.1716613115, 2018.

Stephens, B.B., Gurney, K. R., Tans, P. P., *et al.*:. Weak northern and strong tropical land carbon uptake from vertical profiles of atmospheric CO_2. *Science* **316**: 1732– 35, doi:10.1126/science.1137004. 2007

Stephens, B., et al. 2017. ORCAS Airborne Oxygen Instrument. Version 1.0. UCAR/NCAR - Earth Observing Laboratory. https://doi.org/10.5065/D6N29VC6.

Sweeney, C., Karion, A., Wolter, S., et al.: Seasonal climatology of CO_2 across North America from aircraft measurements in the NOAA/ESRL Global Greenhouse Gas Reference Network. *J. Geophys. Res. Atmos.*, 120, 5155– 5190. doi: 10.1002/2014JD022591. 2015

Suntharalingam, P., Jacob, D.J., Palmer, P.I., Logan, J.A., Yantosca, R.M., Xiao, Y., Evans, M.J., Streets, D.G., Vay, S.L., and Sachse, G.W.: Improved quantification of Chinese carbon fluxes using CO2/CO correlations in Asian outflow, J. Geophys. Res.: Atmos., 109, D18S18, https://doi.org/10.1029/2003JD004362, 2004.

Tramontana, G., Jung, M., Schwalm, C. R., Ichii, K., Camps-Valls, G., Ráduly, B., Reichstein, M., Arain, M. A., Cescatti, A., Kiely, G., Merbold, L., Serrano-Ortiz, P., Sickert, S., Wolf, S., and Papale, D.: Predicting carbon dioxide and energy fluxes across global FLUXNET sites with regression algorithms, Biogeosciences, 13, 4291–4313, https://doi.org/10.5194/bg-13-4291-2016, 2016.

van der Werf, G. R., Randerson, J. T., Giglio, L., Gobron, N., and Dolman, A. J.: Climate controls on the variability of fires in the tropics and subtropics, *Global Biogeochem. Cycles*, 22, GB3028, doi:10.1029/2007GB003122. 2008

Wofsy, S. C.: HIAPER Pole-to-Pole Observations (HIPPO): Fine-grained, global-scale measurements of climatically important atmospheric gases and aerosols, Philos. Trans. R. Soc. A-Math. Phys. Eng. Sci., 369, 2073– 2086, https://doi.org/10.1098/rsta.2010.0313, 2011.

Wofsy, S.C., Afshar, S., Allen, H.M., Apel, E., Asher, E.C., Barletta, B., Bent, J., Bian, H., Biggs, B.C., Blake, D.R., and Blake, N.: ATom: Merged Atmospheric Chemistry, Trace Gases, and Aerosols, ORNL DAAC, Oak Ridge, Tennessee, USA, https://doi.org/10.3334/ORNLDAAC/1581, 2018.

https://doi.org/10.5194/essd-2020-123
Preprint. Discussion started: 7 July 2020

Wunch, D., Toon, G.C., Blavier, J.F.L., Washenfelder, R.A., Notholt, J., Connor, B.J., Griffith, D.W., Sherlock, V., and Wennberg, P.O.: The total carbon column observing network, Philos. Trans. R. Soc. A, 369, 2087-2112, https://doi.org/10.1098/rsta.2010.0240, 2011.

Yang, Z., Washenfelder, R. A., Keppel-Aleks, G., Krakauer, N. Y., Randerson, J. T., Tans, P. P., Sweeney, C., and Wennberg, P. O.: New constraints on Northern Hemisphere growing season net flux, Geophys. Res. Lett., 34, L12807, https://doi.org/10.1029/2007GL029742, 2007.

Yin, Y., Bowman, K., Bloom, A.A., and Worden, J.: Detection of fossil fuel emission trends in the presence of natural carbon cycle variability, Environ. Res. Lett., 14, 084050, https://doi.org/10.1088/1748-9326/ab2dd7, 2019.

Zhu, C., Byrd, R.H., Lu, P., and Nocedal, J.: Algorithm 778: L-BFGS-B: Fortran subroutines for large-scale bound-constrained optimization, ACM Trans. Math. Softw., 23, 550-560, https://doi.org/10.1145/279232.279236, 1997.

https://doi.org/10.5194/essd-2020-123
Preprint. Discussion started: 7 July 2020

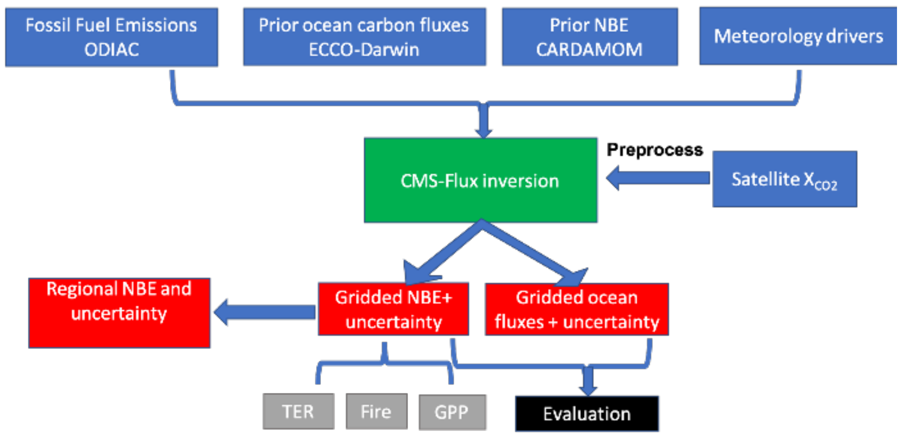

Figure: 1 Data flow diagram with the main processing steps to generate regional net biosphere change (NBE). TER: total ecosystem respiration; GPP: gross primary production. The green box is the inversion system. The blue boxes are the inputs for the inversion system. The red boxes are the data outputs from the system. The black box is the evaluation step, and the grey boxes are the future additions to the product.

https://doi.org/10.5194/essd-2020-123
Preprint. Discussion started: 7 July 2020

Open Access Earth System Science Data Discussions

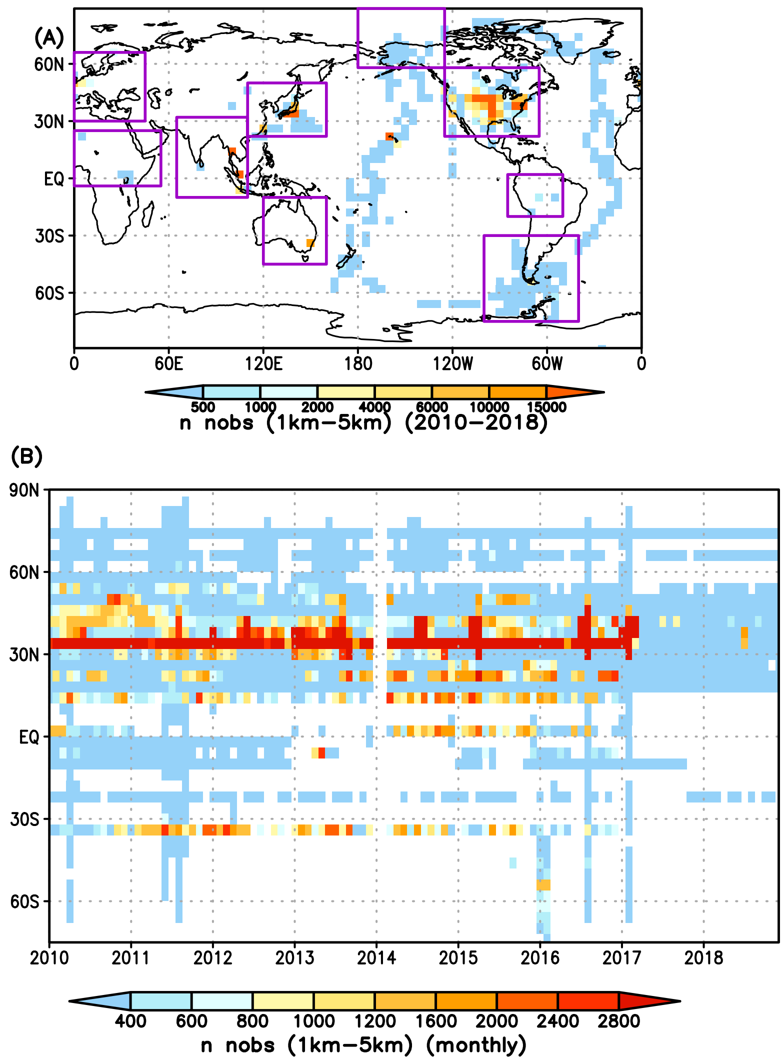

Figure: 2 The spatial and temporal distributions of aircraft observations used in evaluation of posterior NBE. (A) The total number of aircraft observations between 1–5 km between 2010–2018 at each 4° x 5°grid point. The rectangle boxes show the range of the nine sub regions. (B) The total number of monthly aircraft observations at each longitude as a function of time.

https://doi.org/10.5194/essd-2020-123
Preprint. Discussion started: 7 July 2020

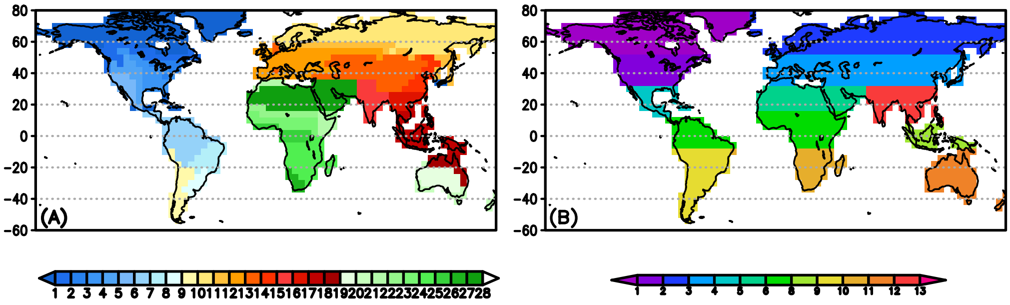

Figure: 3 Two types of regional masks used in calculating regional fluxes. The mask in (A) is based on a combination of condensed seven MODIS IGBP plant functional types, TRANCOM-3 regions (Gurney et al., 2004), and continents. The mask in (B) is based on latitude and continents.

https://doi.org/10.5194/essd-2020-123
Preprint. Discussion started: 7 July 2020

Open Access Earth System Science Data Discussions

1007 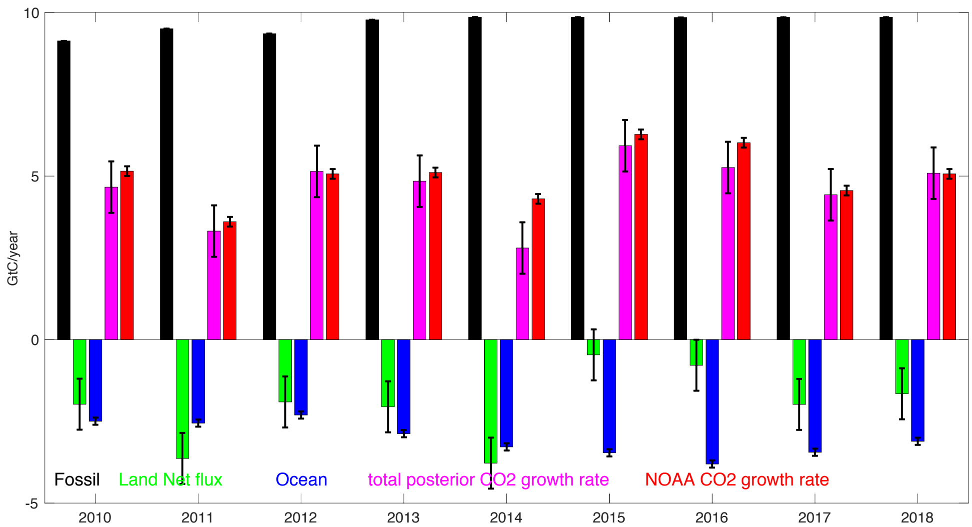

1008 **Figure: 4 Global flux estimation and uncertainties from 2010 –2018 (black: fossil fuel; green:**
1009 **posterior land fluxes; blue: ocean fluxes; magenta: estimated CO_2 growth rate; red: NOAA**
1010 **CO_2 growth rate).**

https://doi.org/10.5194/essd-2020-123
Preprint. Discussion started: 7 July 2020

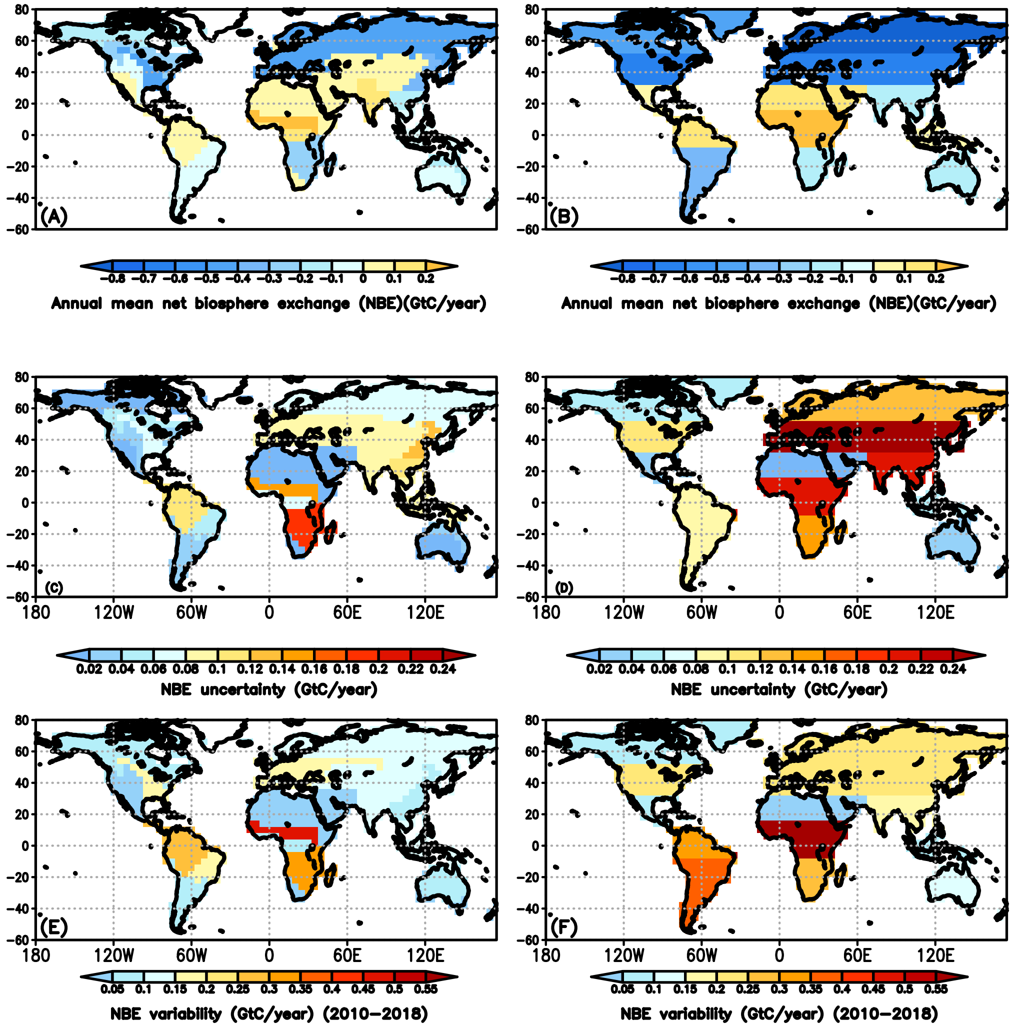

1011

1012 **Figure: 5 Mean annual regional NBE (A and B), uncertainty (C and D), and variability**
1013 **between 2010–2018 (E and F) with two types of regional masks.**

Open Access Earth System Science Data Discussions

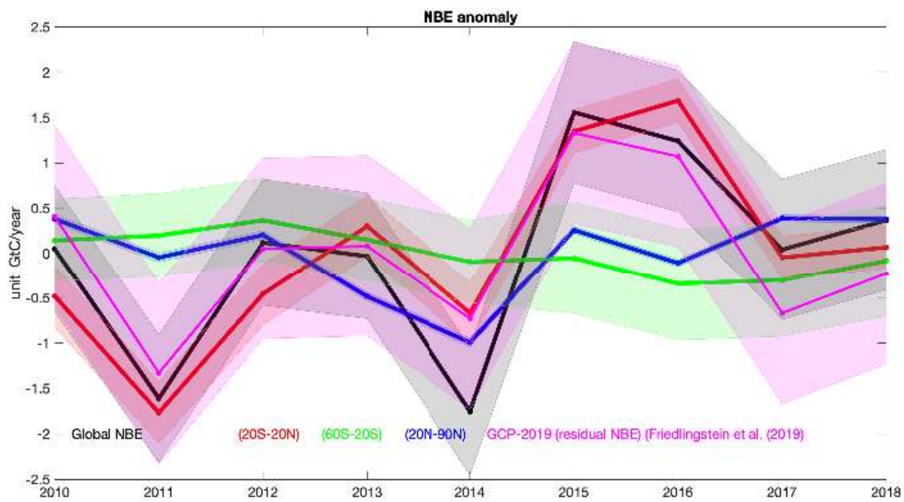

Figure: 6 The NBE interannual variability over the globe (black), the tropics (20°S–20°N), SH mid-latitudes (60°S–20°S), and NH mid-latitudes (20°N–9°0N). For reference, the residual net land carbon sink from GCP (Friedlingstein et al., 2019) and its uncertainty is also shown (magenta).

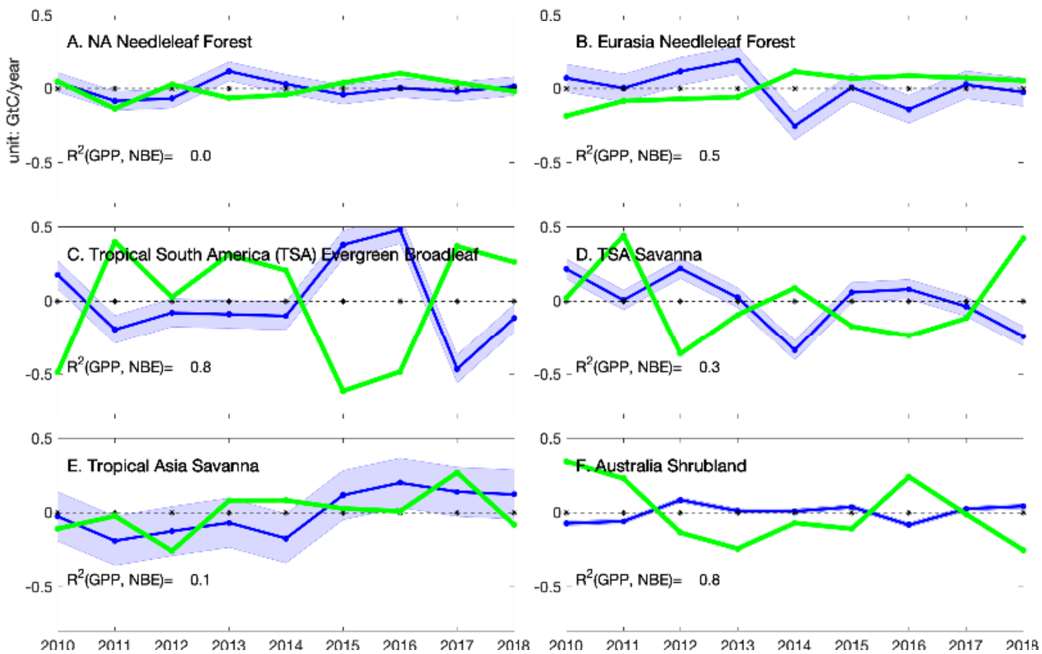

Figure: 7 The NBE interannual variability over six selected regions. Blue: annual NBE anomaly and its uncertainties. Green: annual GPP anomaly based on FLUXSAT.

https://doi.org/10.5194/essd-2020-123
Preprint. Discussion started: 7 July 2020

Open Access Earth System Science Data Discussions

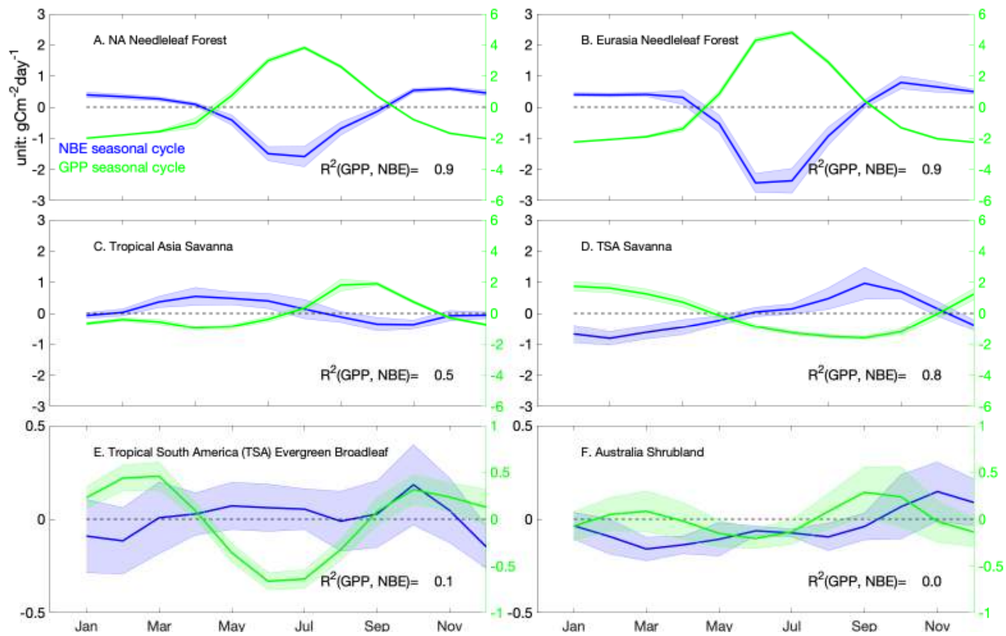

Figure: 8 Blue: climatological NBE seasonality over six selected regions shown in Figure 3A; blue shaded: NBE monthly uncertainty and variability (1-sigma) over nine years. Green and shaded: monthly mean GPP and its variability (1-sigma) over nine years. The names of each region are shown on individual subplots.

https://doi.org/10.5194/essd-2020-123
Preprint. Discussion started: 7 July 2020

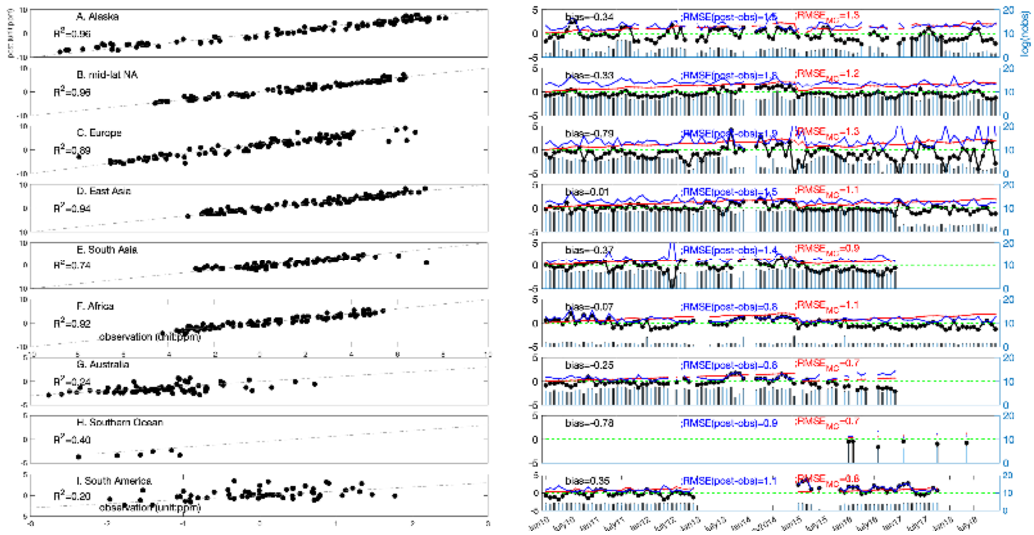

Figure: 9 Comparison between posterior CO_2 mole fraction and aircraft observations. Left panel: detrended posterior CO_2 (y-axis) vs. detrended aircraft CO_2 (x-axis) over nine regions. The dashed line is 1:1 line; right panel: black: the differences between posterior CO_2 and aircraft CO_2 as a function of time; blue: RMSE (unit: ppm); red: $RMSE_{MC}$. The blue bar shows the number of aircraft observations (log scale) as a function of month.

https://doi.org/10.5194/essd-2020-123
Preprint. Discussion started: 7 July 2020

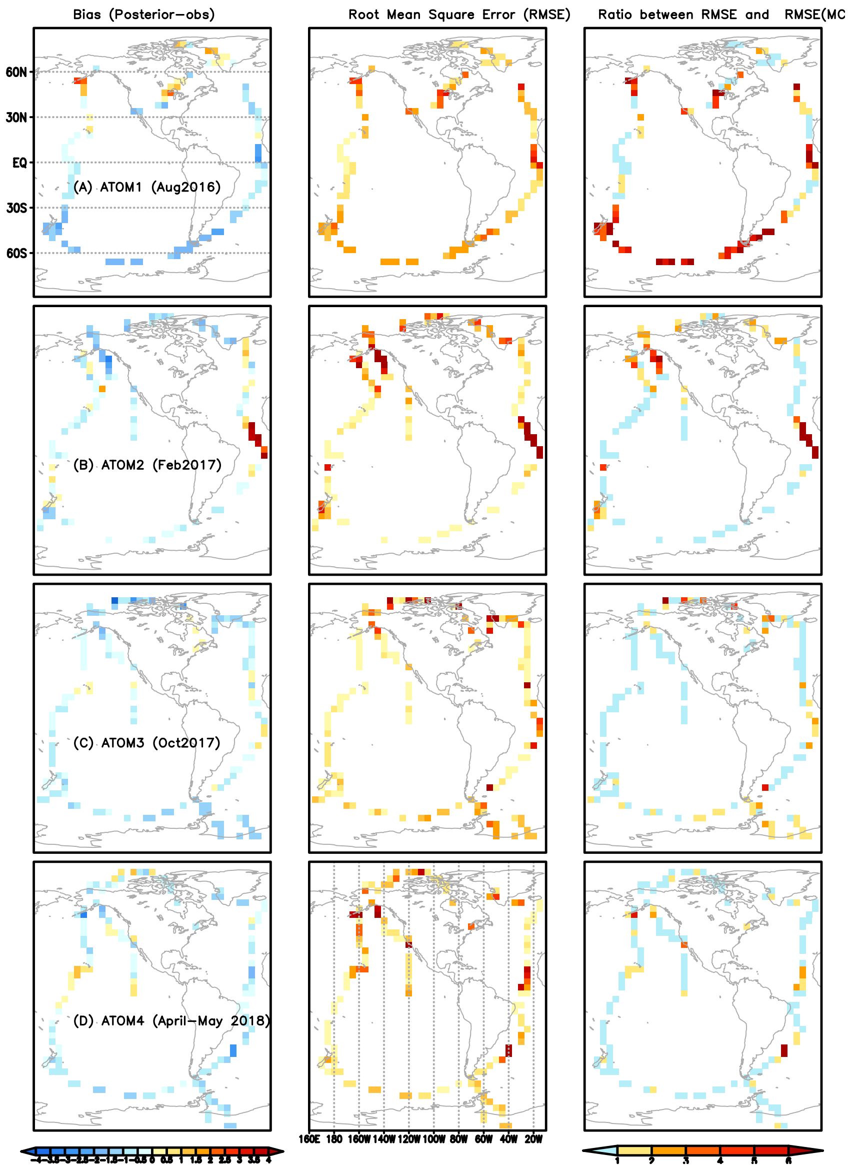

Figure: 10 Left column: the mean differences between posterior CO_2 and aircraft observations from ATOM 1–4 aircraft campaigns between 1–5 km (A–D). Middle column: the Root Mean Square Errors (RMSE) between aircraft observations and posterior CO_2 between 1–5 km. The color bar is the same as the left column. Right column: the ratio between RMSE and $RMES_{MC}$ based on ensemble CO_2 from the Monte Carlo uncertainty estimation method.

https://doi.org/10.5194/essd-2020-123
Preprint. Discussion started: 7 July 2020

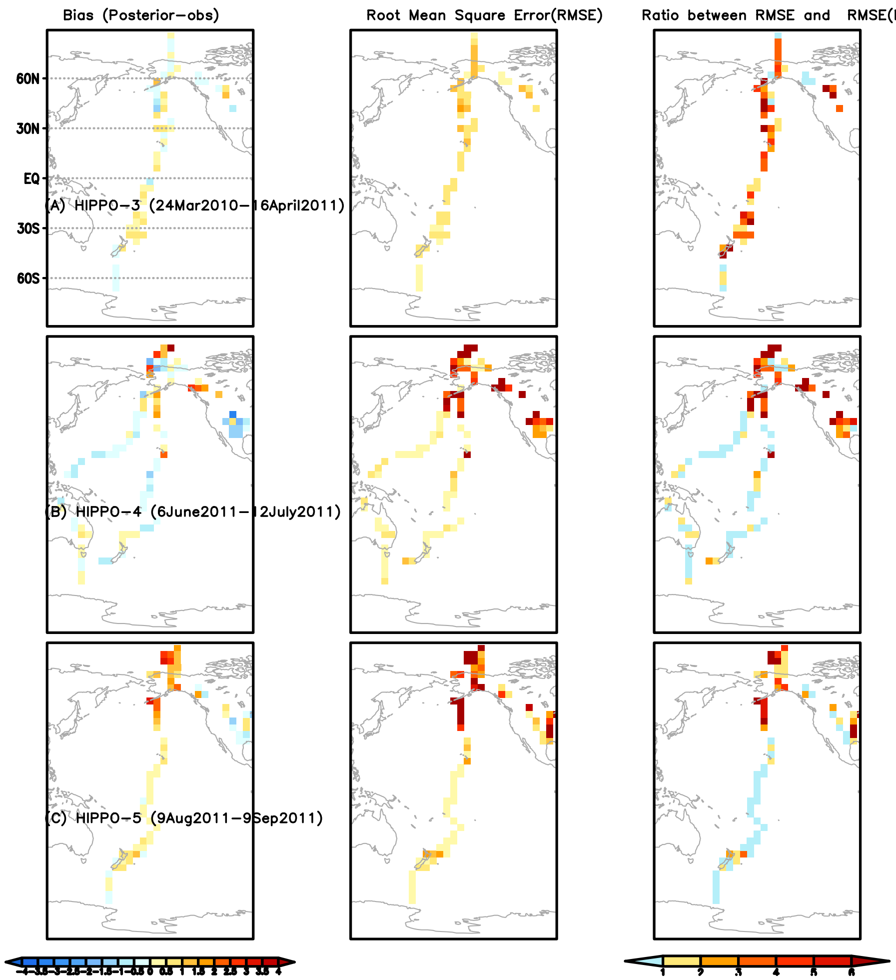

Figure: 11 Left column: the mean differences between posterior CO_2 and aircraft observations from HIPPO 3-5 aircraft campaigns between 1–5 km (A–C) (unit: ppm). (unit: ppm). The time frame of each campaign is in the figure. Middle column: the Root Mean Square Errors (RMSE) between aircraft observations and posterior CO_2 between 1–5 km (unit: ppm). The color bar is the same as the left column. Right column: the ratio between RMSE and $RMSE_{MC}$ based on ensemble CO_2 from the Monte Carlo method.

https://doi.org/10.5194/essd-2020-123
Preprint. Discussion started: 7 July 2020

Table: 1 Configurations of the CMS-Flux atmospheric inversion system

	Model setup	Configuration	Reference
Inversion general setup	Spatial scale	Global	--
	Spatial resolution	4° latitude x 5° longitude	
	Time resolution	monthly	
	Minimizer of cost function	L-BFGS	Byrd et al., 1994; Zhu et al., 1997
	Control vector	Monthly net terrestrial biosphere fluxes and ocean fluxes	
Transport model	Model name	GEOS-Chem and its adjoint	Suntharalingam et al., 2004 Nassar et al., 2010 Henze et al., 2007
	Meteorological forcing	GEOS-5 (2010–2014) and GEOS-FP (2015–2019)	Rienecker et al., 2008

https://doi.org/10.5194/essd-2020-123
Preprint. Discussion started: 7 July 2020

Table: 2 Description of the prior fluxes and assumed uncertainties in the inversion system

Prior fluxes	**Terrestrial biosphere fluxes**	**Ocean fluxes**	**Fossil fuel emissions**
Model name	CARDAMOM-v1	ECCO-Darwin	ODIAC 2018
Spatial resolution	4° x 5°	0.5°	1° x 1°
Frequency	3-hourly	3-hourly	hourly
Uncertainty	Estimated from CARDAMOM	100% same as Liu et al. (2017)	No uncertainty
References	Bloom et al., 2006; 2020	Brix et al, 2015; Carroll et al., 2020	Oda et al., 2016; 2018

https://doi.org/10.5194/essd-2020-123
Preprint. Discussion started: 7 July 2020

Table: 3 Description of observation and evaluation dataset. Data sources are listed in Table 7.

	Dataset name and version	References
Satellite X_{CO2}	ACOS-GOSAT v7.3	O'Dell et al., (2012)
	OCO-2 v9	O'Dell et al., (2018)
Aircraft CO_2 observations	ObsPack OCO-2 MIP	CarbonTracker team (2019)
	HIPPO 3-5	Wofsy et al. (2011)
	ATOM 1-4	Wofsy et al.(2018)
	INPE	Gatti et al., (2014)
	ORCAS	Stephens et al., 2017
GPP	FLUXSAT-GPP	Joiner et al., (2018)

https://doi.org/10.5194/essd-2020-123
Preprint. Discussion started: 7 July 2020

Open Access Earth System Science Data Discussions

Table: 4 Latitude and longitude ranges for seven sub regions.

Region	**Alaska**	**Mid-lat NA**	**Europe**	**East Asia**	**South Asia**
Longitude range	180°W–125° W	125°W–65°W	5°W–45°E	110°E–160°E	65°E–110°E
Latitude range	58°N–89°N	22°N-58°N	30°N–66°N	22°N–50°N	10°S–32°N
Region	Africa	South America	Australia	Southern Ocean	
Longitude range	5°W–55°E	95°W–50°W	120°E–160°E	110°W–40°E	
Latitude range	2°N–18°N	20°S–2°N	45°S–10°S	80°S–30°S	

Table: 5 List of the data products.

Product	Spatial resolution	Temporal resolution when applicable	Data format	Sample data description in the text
Total fossil fuel, ocean, and land fluxes	Global	Annual	*csv*	Figure 4 (section 4.1)
Climatology mean NBE, variability, and uncertainties	PFT and continents based 28 regions	N/A	*csv*	Figure 5 (section 4.2)
	Geographic-based 13 regions		*csv*	
Hemispheric NBE and uncertainties	NH (20°N-90°N), tropics (20°S-20°N), and SH (60°S-20°S)	Annual	*csv*	Figure 6 (section 4.3)
NBE variability and uncertainties	PFT and continents based 28 regions	Annual	*csv*	Figure 7 (section 4.3)
	Geographic -based 13 regions		*csv*	
NBE seasonality and its uncertainties	PFT and continents based 28 regions	Monthly	*csv*	Figure 8 (section 4.4)
	Geographic -based 13 regions		*csv*	
Monthly NBE and uncertainties	PFT and continents based 28 regions	Monthly	*csv*	N/A
	Geographic -based 13 regions		*csv*	
Gridded NBE and uncertainties	4° (latitude) x 5° (longitude)	Monthly	*NetCDF*	N/A
Region masks	PFT and continents based 28 regions	N/A	csv	Figure 3 (section 2.4)
	Geographic -based 13 regions		csv	
Fluxes at a few selected flux tower sites		Monthly	*csv*	N/A

https://doi.org/10.5194/essd-2020-123
Preprint. Discussion started: 7 July 2020

Table: 6 The nine-year mean regional annual fluxes, uncertainties, and variability. Regions are based on the mask shown in Figure 5A (Figure 5.csv). Unit: GtC/year

Region name (Figure4.csv)	Mean NBE	Uncertainty	Variability
NA shrubland	-0.14	0.02	0.05
NA needleleaf forest	-0.22	0.04	0.06
NA deciduous forest	-0.2	0.04	0.07
NA crop natural vegetation	-0.41	0.06	0.18
NA grassland	-0.04	0.03	0.03
NA savannah	0.03	0.02	0.03
Tropical South America (SA) evergreen broadleaf	0.04	0.1	0.28
SA savannah	-0.09	0.06	0.18
SA cropland	-0.07	0.03	0.07
SA shrubland	-0.03	0.02	0.08
Eurasia shrubland savanna	-0.44	0.07	0.14
Eurasia needleleaf forest	-0.41	0.07	0.12
Europe cropland	-0.46	0.09	0.16
Eurasia grassland	0.02	0.08	0.13
Asia cropland	-0.37	0.13	0.08
India	0.14	0.09	0.14
Tropical Asia savanna	-0.12	0.11	0.08
Tropical Asia evergreen broadleaf	-0.09	0.09	0.12
Australia (Aus) savannah grassland	-0.11	0.02	0.09
Aus shrubland	-0.07	0.01	0.05
Aus cropland	-0.01	0.01	0.03
African (Afr) northern shrubland	0.04	0.02	0.03
Afr grassland	0.03	0.01	0.01
Afr northern savanna	0.54	0.15	0.49
Afr southern savanna	-0.27	0.18	0.33
Afr evergreen broadleaf	0.1	0.07	0.09
Afr southern shrubland	0.01	0.01	0.01
Afr desert	0.06	0.01	0.04

https://doi.org/10.5194/essd-2020-123
Preprint. Discussion started: 7 July 2020

Table: 7 Lists of data sources used in producing and evaluating posterior NBE product.

Data name	Data Source
ECCO-Darwin ocean fluxes	https://data.nas.nasa.gov/ecco
CARDAMOM NBE and uncertainties	https://doi.org/10.25966/4v02-c391
ODIAC	http://db.cger.nies.go.jp/dataset/ODIAC/DL_odiac2019.html
GOSAT b7.3	https://oco2.gesdisc.eosdis.nasa.gov/data/GOSAT_TANSO_Level2/ACOS_L2S.7.3/
OCO-2 b9	https://disc.gsfc.nasa.gov/datasets?page=1&keywords=OCO-2
ObsPack	https://www.esrl.noaa.gov/gmd/ccgg/obspack/data.php
ATom 1-4	https://daac.ornl.gov/ATOM/guides/ATom_merge.html
HIPPO 3-5	https://www.eol.ucar.edu/field_projects/hippo
INPE	https://www.esrl.noaa.gov/gmd/ccgg/obspack/data.php?id=obspack_co2_1_INPE_RESTRICTED_v2.0_2018-11-13 and
FLUXSAT-GPP	https://gs614-avdc1-pz.gsfc.nasa.gov/pub/tmp/FluxSat_GPP/
Posterior NBE	https://doi.org/10.25966/4v02-c391